5-2016

COMPUTATIONAL AND EXPERIMENTAL INVESTIGATIONS TOWARDS IMPROVING ORGANIC AND DYE-SENSITIZED SEMICONDUCTOR SOLAR CELLS

Nathan D. Colley
ndcolley7@siu.edu

COMPUTATIONAL AND EXPERIMENTAL INVESTIGATIONS TOWARDS IMPROVING ORGANIC AND DYE-SENSITIZED SEMICONDUCTOR SOLAR CELLS

by

Nathan D. Colley

A Thesis
Submitted in Partial Fulfillment of the Requirements for
Chemistry Honors and ACS Certification

Department of Chemistry and Biochemistry
Southern Illinois University Carbondale
May 2016

AN ABSTRACT OF THE THESIS OF

Nathan D. Colley, for Chemistry Honors and ACS Certification

TITLE: COMPUTATIONAL AND EXPERIMENTAL INVESTIGATIONS TOWARDS IMPROVING ORGANIC AND DYE-SENSITIZED SEMICONDUCTOR SOLAR CELLS

MAJOR PROFESSOR: DR. LICHANG WANG

The global energy consumption is expected to double by 2050. Therefore, alternative energy sources such as solar power will have to be utilized. This work seeks to improve next generation solar cells, namely organic solar cells (OSCs) and dye-sensitized semiconductor solar cells (DSSCs), using theoretical and experimental approaches. Computational studies were done on electron acceptor and electron donor molecules that have potential use in OSCs and DSSCs. An improved Density Functional Theory (DFT) method that better represents experimental cyclic voltammetry was developed to predict the electronic properties of these molecules. The electronic data of the electron acceptor molecules were used to design OSCs by matching cascading HOMO and LUMO energy levels with a known donor molecule. Absorption spectra were generated using Time-Dependent DFT (TD-DFT) calculations. The effect of functional group on the accuracy of DFT and TD-DFT calculations was also studied in electron donor molecules. It was found that the prediction accuracy of the electronic properties increases as the electron withdrawing ability of the functional group increases, while the accuracy of the predicted absorption spectra decreases as the electron withdrawing ability of the functional group increases. OSCs and DSSCs were fabricated using coal dye solutions as a photosensitizer. The electrical output of these solar cells was tested and the efficiency of each solar cell device was calculated. It was found that the use of coal gave significantly better results than the blank. Therefore, coal dye solutions can be utilized as potential photosensitizers in these devices.

ACKNOWLEDGMENTS

Firstly, I would like to thank Dr. Lichang Wang allowing me to join her group and start research my freshman year. I am incredibly grateful for her guidance and expertise over the past four years. Doing research with Dr. Wang has been one of the best experiences of my undergraduate career and has influenced me to pursue my PhD. in Chemistry and continue solar research. I would also like to thank Dr. Pamela Ubaldo for her guidance and patience with me when I first began doing research. I also wish to thank Dr. Qingfeng Ge and Krishanthi Weerasinghe for their help and advice on my projects.

TABLE OF CONTENTS

LIST OF TABLES

LIST OF FIGURES

CHAPTER 1
INTRODUCTION

1.1 Call for renewable energy

Renewable energy will be a necessity of future society. Current global energy production relies heavily on the burning of fossil fuels, which are in limited supply. Some models estimate that oil and natural gas reserves will be completely diminished by 2042 and coal reserves will only last until 2112[1]. Global energy consumption has increased significantly over the last four decades[2]. In 2004, the global energy consumption was 14.5 terawatts (TW), which is the equivalent of burning 220 million barrels of oil every day[3]. By 2050, this number is expected to be around 30 TW[4]. However, if all 10 billion people on Earth in 2050 are to use only an average of two kilowatt-hours per person, the global energy need would be about 60 TW, which is the equivalent of burning of 900 million barrels of oil per day[3].

In addition to their limited supply, it is widely accepted by the scientific community that the burning of fossil fuels contributes to global warming or climate change through the Greenhouse Effect[5]. There is strong evidence that suggests climate change will have detrimental effects on the environment, economy, and human health[5-10]. Scientists predict that global warming will be the culprit for an increase in the frequencies of severe thunderstorms[6], costal erosion[7], droughts[8], and hurricanes[9]. Scientists also predict that global warming will have adverse effects on human health through elevated risks of thermal stress and infectious diseases spread by insects, such as malaria and dengue fever[10].

The need for renewable energy is obvious, but where will this energy come from? In order to gain a better understanding of how the energy of the future will be produced, it is important to understand how energy is generated today. It can be seen in Figure 1 that 81.4% of

the world total primary energy supply (TPES) in 2013 was from fossil fuels. Nuclear, hydroelectric, and biofuels accounted for 17.4% of the 2013 TPES. Solar, wind, and geothermal energy made up only a small fraction, 1.2%, of the 2013 TPES. The TPES percentage from solar, wind, and geothermal has seen a 12 fold increase over the past 40 years, but there is still a great deal of potential for growth[2]. Solar power accounts for about 0.015% for the TPES, which is about 0.2 TW[11]. This is miniscule compared to the 120,000 TW continuously striking Earth[4, 11]. Only 0.025% of this power would need to be harvested to satisfy the 30 TW need using solar energy.

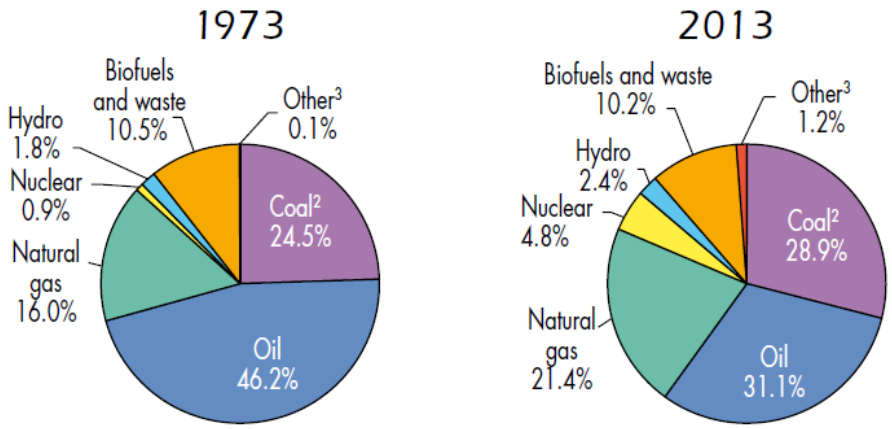

Figure 1. 1973 and 2013 fuel shares of total primary energy supply[2].

It is highly unlikely that the energy produced in 2050 will come from a single source. Ideally, fossil fuels will only make up a minor portion of future energy production and the majority of it will come from a combination of renewable energy sources. Biofuels currently hold the largest portion of the TPES for any renewable energy. However, biofuels must overcome serious issues before becoming a suitable candidate to replace fossil fuels. It has been estimated that 35% of the total U.S. land area would need to be utilized as farmland in order to obtain 1 TW from corn ethanol using current technology[12]. There are also concerns that using

crops as a fuel source could lead to food and water shortages and the degradation of forests[13]. Nuclear energy may seem to be a promising future energy source. However, in order to generate enough power for the 2050 need, a 1 GW nuclear fission power plant must be built every day for the next 50 years[14]. To put this into perspective, there are currently 438 nuclear reactors in the world, 99 of which are in the United States[15-16]. It is unlikely that a significant amount of hydroelectric energy will be added because most of the available hydroelectric energy sources have already been utilized[3]. Wind energy may also be a promising renewable energy source in the future. It has been estimated that the total globally extractable wind power is 2-6 TW[17]. However, a major concern with wind energy is the scarcity of materials. In order to build enough magnets for the generators in enough wind turbines capable of producing 1 TW, it would take 40 years production of neodymium and 50 years production of dysprosium[12].

Solar energy has become one of the most attractive alternative energy options because of the seemingly infinite energy provided by the sun: 36,000 TW on land[18]. Only a fraction of this power needs to be captured to satisfy the 2050 power need. Nate Lewis from the California Institute of Technology proposes that only 60,000 km^2 of 15% efficient solar panels would be needed to solve the 30 TW demand. His proposed solution is shown in Figure 2; each box is located in an area of high solar radiation and has the dimensions 100 km x 100 km^3. Although solar production has grown, this simplistic solution is far from being realized because the cost to produce solar energy is still high compared to other energy sources[3, 19]. This limitation has given motivation for solar cell research, which has led to the development of many new types of solar cells in the hopes lowering production cost and raising solar cell efficiency. This thesis will focus on organic and dye-sensitized solar cells, both of which utilize organic based molecules as the photoactive material.

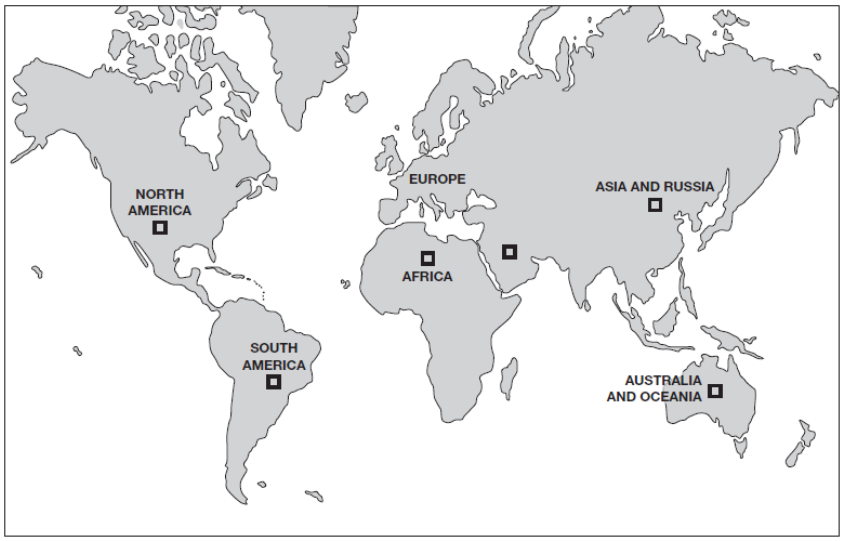

Figure 2. Map of the solar cell land requirement to achieve 30 TW of power using 15% solar cells. Each box is 100 km x 100 km. [3]

1.2 Solar cells utilizing organic materials as photosensitizers

Organic and dye-sensitized solar cells are emerging classes of thin film photovoltaics that offer potential advantages over traditional silicon solar cells. Both types of solar cells have lower production costs due to the mild processing conditions. These solar cells can also be made using flexible, lightweight and highly transparent materials, which will allow them to be easily integrated into consumer products and building architecture[20-32].

1.2.1 Organic solar cells

Organic solar cells (OSC) or organic photovoltaics (OPV) are typically divided into two classes: polymer organic solar cells and small-molecule organic solar cells. Moreover, devices can also be made using a combination of polymers and small molecules[22]. OSCs are generally composed of donor and acceptor layers between a conductive glass oxide anode and a metal

cathode. If the donor and acceptor layer are separated, the device is known as a bilayer heterojunction OSC. Conversely, if the donor and acceptor are mixed, the device is known as a bulk heterojunction OSC[22, 24, 31]. The general design of both types of devices is depicted in Figure 3.

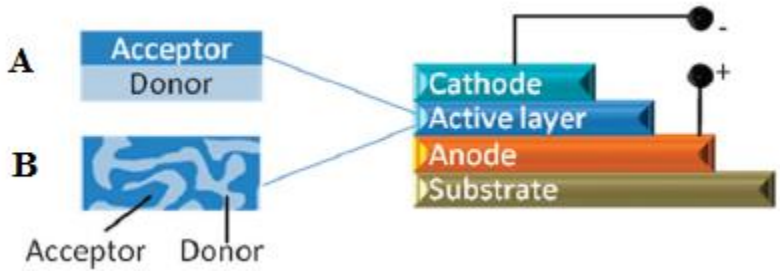

Figure 3. General design of A) bilayer heterojunction OSC B) bulk heterojunction OSC[24]

Some common electron donor molecules include conjugated polymers, fused acenes, oligothiophenes, triphenyl amine based molecules, and dye-based molecules (phthalocyanine, diketopyrrolopyrroles, etc.)[22-24]. Common electron acceptor molecules include fullerenes and fullerene derivatives such as phenyl-C_{61}-butyric acid methyl ester (PCMB) and cyclopenta-fused polycyclic aromatic hydrocarbons (CP-PAHs)[22-24, 33]. The donor molecules are the hole transporting material and the acceptor molecules are the electron transporting material[31]. The anode and cathode materials are usually indium tin oxide (ITO) and aluminum respectively[24]. Gold, silver, and calcium have also been used as cathodes in OSCs[29].

The working principle of an OSC is shown in Figure 4. In the first step an incident photon is absorbed, creating a Frenkel exciton[28-29, 31]. This excites an electron from HOMO to LUMO in the donor layer. The electrons are then injected into the slightly lower energy LUMO of the acceptor layer, which then quickly travels to the anode. At the same time, the hole

migrates from the donor layer to the cathode[29]. If the anode and cathode are connected by an external wire, the charge transfer can be used to do work on a load.

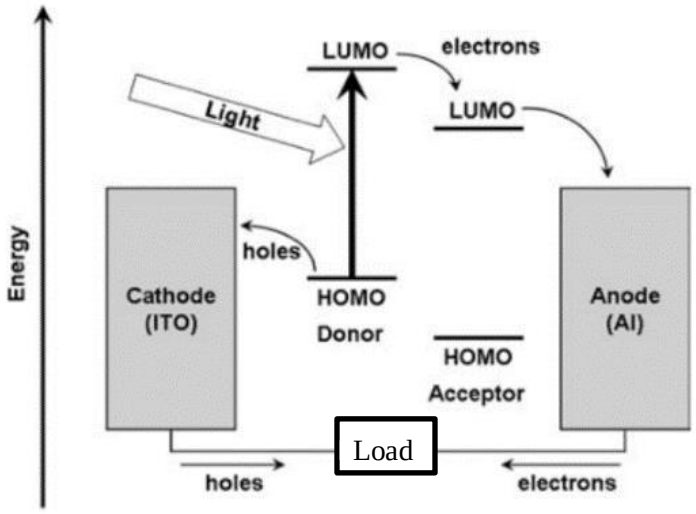

Figure 4. Working principle of bilayer heterojunction organic solar cell. Adapted from ref.[29]

1.2.2 Dye-sensitized solar cells

Dye-sensitized semiconductor solar cells (DSSCs) are a promising type of thin-film solar cells belonging to the third generation of photovoltaics[20, 27]. DSSCs use natural or synthetic dyes covalently bonded[32] to the surface of a wide band gap semiconductor to harvest light. The dye, which is arguably the most important component of DSSCs, can range from organic molecules found in nature to synthetic metal complexes with organic ligands to organic molecules made in the lab[20-21, 26-27, 30, 32]. Ruthenium complexes were considered to be the best dyes for many years. However, the toxicity and scarcity of ruthenium has led researchers to develop metal-free organic dyes, which can be economically viable and easily synthesized[30, 32].

DSSCs are composed of five components: conductive glass substrate, anode, active dye layer, electrolyte, and cathode[20-21, 26-27, 30, 32]. The conductive glass substrate is made by depositing a layer of transparent conductive oxide such as indium tin oxide (ITO) or fluorine-doped tin oxide (FTO) on glass. The resulting conductive glass substrate has a resistance of about 15 Ω[20]. The anode is a layer of wide band gap semiconductor deposited on the conductive glass substrate. The most common anode is anatase TiO_2[20, 30]. As mentioned previously, the dye layer is covalently bonded to the anode and can be organic or a metal-organic complex. The electrolyte in DSSCs in typically the iodide/tri-iodide (I^-/I_3^-) red/ox couple[30]. The most common cathode material is platinized conducting glass[21, 32], but cheaper carbon counter electrodes have also been studied[21, 34]. The general design and working principle of a DSSC is shown in Figure 5.

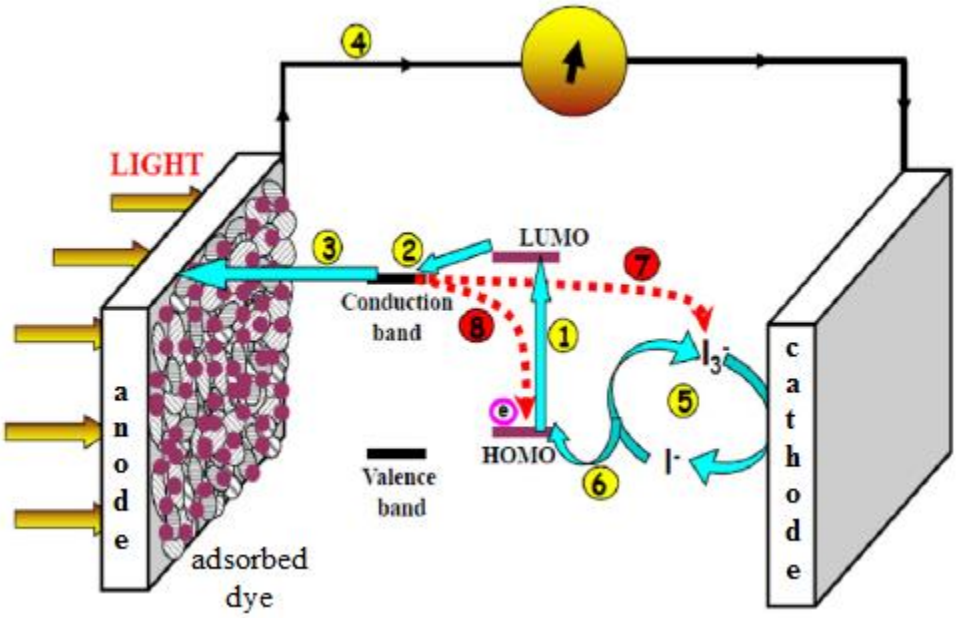

Figure 5. Working principle of a dye-sensitized solar cell. Adapted from ref[27].

In Step 1, an incident photon is absorbed to excite an electron in the dye from HOMO to LUMO. The electron is injected into the lower energy conduction band of the metal oxide semiconductor in Step 2. Next, the electron is transferred from the metal oxide layer to the

transparent conducting glass substrate. In Step 4, the electron travels via an external wire from the anode to cathode. Next, the electron migrates from the cathode to the electrolyte red/ox couple. In step 5, tri-iodide is reduced to iodide. In Step 6, iodide is oxidized back to tri-iodide while simultaneously reducing the dye back to the neutral state[20, 27]. Step7 and Step 8 illustrate unfavorable charge recombinations in which the tri-iodide electrolyte or the oxidized dye molecule are reduced by the photo-excited electron without completing the circuit[27].

1.3 Ideal photosensitizer materials

There are several factors to consider when choosing photosensitizer materials for OSCs and DSSCs. Some of these factors include production costs, ease of synthesis, molar absorption coefficient, band gap, molecular energy levels, and solubility in a desired solvent[28, 30, 32]. It is hard to generalize the best photosensitizer properties for all OSCs and DSSCs because one must consider the materials of all components used in a particular device. This section briefly sets general guidelines for choosing photosensitizers to design OSCs and DSSCs, although it is likely no one material will possess all of the ideal properties.

1.3.1 Ideal OSC active layer properties

When designing binary OSCs (donor and acceptor active layer), the HOMO of the acceptor molecule should be lower in energy than the HOMO of the donor molecule. Similarly, the LUMO of the acceptor molecule must be lower in energy than the LUMO of the donor molecule[22, 28, 31]. If the frontier orbitals of the acceptor molecule are higher in energy than the frontier orbitals of the donor molecule, the whole exciton will be transferred from donor to

acceptor rather than dissociating between the cathode and acceptor[22]. In order to obtain adequate charge separation, the HOMO and LUMO of the acceptor should be 0.2-0.3 eV lower than the HOMO and LUMO of the donor[28].

1.3.2 Ideal photosensitizers for DSSCs

In addition to absorbing light, arguably the most important property of the dye photosensitizer in DSSCs is its ability to be adsorbed on the semiconducting metal oxide layer. The adsorption of the dye to the metal oxide surface is crucial for generating electrical current; it allows the injection of electrons from the dye into the conduction band of the metal oxide. Adsorption occurs via interactions between the metal oxide surface and certain functional groups known as "anchoring groups". The anchoring groups of dye molecules are mainly adsorbed on the metal oxide surface through covalent bonding and hydrogen bonding[26].

The most commonly used anchoring group is the carboxylic acid (-COOH) functional group[20]. However, a variety of anchoring groups has been studied recently including phosphonic acid ($-PO_3H_2$), nitro ($-NO_2$) and pyridine ($-C_5H_4N$)[26]. The hydroxyl (-OH) and carbonyl (-CO) functional groups also act as anchoring groups in many natural dye molecules studied for use in DSSCs[35]. Although these anchoring groups vary in chemical identity, they all can form covalent bonds with the metal oxide surface. Without anchoring groups, the dye molecule would not be immobilized on the metal oxide surface and electrons would not easily be transferred from dye to metal oxide. Therefore, when designing molecules for DSSCs, it is essential that the dye contains at least one anchoring group.

CHAPTER 2
DFT STUDIES ON THE OPTOELECTRONIC PROPERTIES OF ORGANIC MOLECULES

2.1 Overview of DFT

Density Functional Theory (DFT) has become one of the most widely used methods for the calculation of the ground-state properties of electronic systems[36-37]. DFT has many applications in science and technology including studies on solar energy harvesting and conversion, inorganic and enzymatic catalysis, drug design, and crystallization of phase change materials[38-39]. The central theme in DFT is that it replaces the many-body electronic wavefunction in the Schrodinger equation in Equation 1 with the electron density[37, 40]. The electron density is function of only three variables and is much simpler than a wavefunction that contains 3N variables, where N is the number of electrons in the system. In DFT, the electron correlation is included indirectly from the outset[40].

$$\hat{\mathrm{H}}\Psi = E\Psi \qquad (1)$$

Modern DFT is governed by two theorems set forth by Hohenberg and Kohn. The first theorem declares that the ground-state electron density determines the electronic wavefunction, and therefore all ground-state properties of an electronic system. The second theorem states that the energy of an electron distribution can be described as a functional of the electron density, and this functional is a minimum for the ground-state. Although these theorems allow us to circumvent the many-body Schrodinger equation, they give rise to a new problem of attempting to minimize the density functional. The Kohn-Sham approach is generally utilized in modern DFT. It relies on the construction of noninteracting systems to give the same density as the original problem. The form of the kinetic energy functional of noninteracting systems is known

exactly, but the exchange and correlation functionals are only known for the free electron gas. However, there exist many approximations that allow the calculation of molecular properties with various levels of accuracy[40].

2.2 Computational details

The computational chemistry software Gaussian09 [41] was used to study the electronic properties and absorption spectra of cyclopentafused polycyclic aromatic hydrocarbons (CP-PAHs) and methyl triphenyl amine (MTPA) based molecules. Optimization, frequency, and absorption spectrum calculations were done in solution phase and carried out using either the 6-311g (d,p) basis set (CP-PAHs) or 6-31g+(d,p) basis set (MTPA). All geometry optimizations followed convergence criteria for SCF, gradient and energy of 10^{-8}, 10^{-6}, and 10^{-6} a. u. respectively. The solvent for each molecule calculated was chosen to match the solvent used in the experimental data. All calculated properties were compared to the available experimental data from references[33, 42-46] and the accuracy of each functional was evaluated by calculating the mean absolute error (MAE).

The majority of the CP-PAH and MTPA calculations were carried out by Dr. Pamela Ubaldo. I did calculations on CP-PAH **1** and **2** with various ether functional groups in the --R position with different alkyl chain lengths. I also performed many DFT and TD-DFT calculations on CP-PAH **5-8** using several basis sets. I also carried a small amount of DFT and TD-DFT calculations on MTPA derivatives that were not completed when I began working on the project. Additionally, I assisted with the data analysis and construction of tables and figures for the CP-PAH and MTPA calculations.

2.2.1 Electronic properties

Accurate predictions of the energies of the highest occupied molecular orbital (HOMO), the lowest unoccupied molecular orbit (LUMO), and HOMO-LUMO bandgap (ΔE_{gap}) are very important when designing OSCs. These energy levels are usually calculated by optimizing the neutral molecule and typically found experimentally using cyclic voltammetry. However, there are often significant discrepancies between the calculated energies and the observed experimental energies. In their study on CP-PAHs, Wood et al. found that the calculated ΔE_{gap} using B3LYP correlation functional with 6-311G(d,p) basis set was 0.25 eV or greater than the ΔE_{gap} found using cyclic voltammetry[33].

Under initial consideration, one may attribute such discrepancies to the flaws in DFT theory or the functional used. However, closer examination of the experimental system compared to the conventional theoretical model provides a reasonable explanation as to why such discrepancies occur. In cyclic voltammetry, the LUMO energy levels are measured by adding an additional electron to the LUMO[33]. However, when using the conventional theoretical method to calculate the LUMO energy of the neutral molecule, no electron is added to the system. One would expect the LUMO energy in the neutral molecule to be higher than the LUMO of the negatively charged molecule. Thus, in order to make a true comparison between the calculated and experimental LUMO and $\Delta E_{gap,}$ the LUMO of the negatively charged species should be calculated[47].

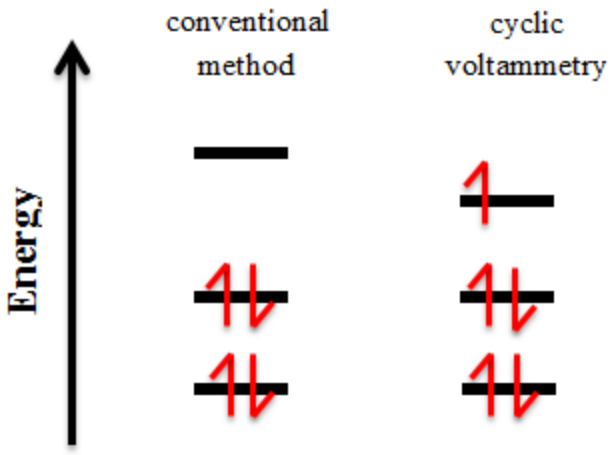

Figure 6. Comparison of LUMO energy levels for conventional DFT calculations and experimental cyclic voltammetry

Note that in cyclic voltammetry, the HOMO energy level is found from the neutral species. Therefore, it has been proposed that the HOMO energy be calculated from the optimized neutral (0) species and the LUMO be calculated from the optimized anionic (-1) species. The HOMO-LUMO energy gap is found by taking the difference between the anionic LUMO and the neutral HOMO[47]. This method will be referred to as the current or improved method throughout this thesis.

In our study on CP-PAHs, six density functionals (B3LYP, CAMB3LYP, HSEH1PBE, PBE, TPSS, HCTH) were used with the 6-311g (d,p) basis set for the DFT calculations of both the neutral and anionic species. In our study on MTPA derivatives, ten density functionals (B3LYP, B3PW91, HSEH1PBE, MPW1PW91, CAM-B3LYP, ωB97XD, BPV86, PBE, TPSS, and HCTH) were used with the 6-31g+(d,p) basis set for the DFT calculations of the neutral and anionic species. The results from the conventional and improved methods for each functional were compared to experimental data and the best method and functionals were determined.

2.2.2 Absorption spectra

The absorption spectrum for each molecule was generated by performing Time Dependent DFT (TD-DFT) calculations on the optimized neutral structure of each molecule. The same functionals and basis sets used in the electronic structure calculations of CP-PAHs and MTPA derivatives were used. For example, the absorption spectrum generated from TD-B3LYP employed a TD-DFT calculation on the optimized neutral structure from B3LYP calculation. In addition to matching the DFT functionals for TD-DFT calculations, a hybrid method was employed. TD-CAMB3LYP calculations were done on structures optimized using B3LYP. This hybrid method is referred to as B3LYP/TD-CAMB3LYP throughout this thesis. The results from each TD-DFT method were compared to experimental data and the best methods were determined.

2.3 Electronic and optical properties of CP-PAHs

CP-PAHs are a class of electron acceptors that have potential use in OSCs[33, 47]. The electronic and optical properties of eight CP-PAHs shown in Figure 7 were calculated *in-silico* and compared to experimental data. The electronic properties were calculated using the conventional and improved DFT methods using B3LYP, CAMB3LYP, HSEH1PBE, PBE, TPSS, and HCTH density functionals with the 6-311g (d,p) basis set. The absorption spectra were generated from TD-DFT calculations. The solvent for molecules **1-5** was tetrahydrofuran (THF) and the solvent for molecules **6-8** was acetonitrile[47].

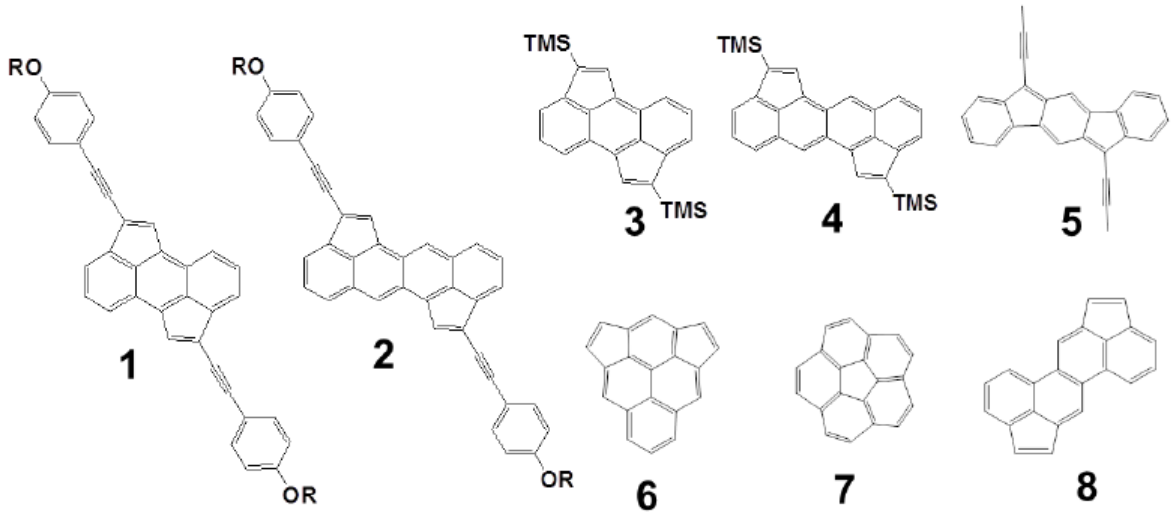

Figure 7. CP-PAH structures[47]: (**1**) 2,7-bis((4-(alkoxy-)phenyl)-ethynyl)cyclopenta[hi]aceanthrylene (R=H, CH_3,C_2H_5, C_3H_7); (**2**) 2,8-bis((4-alkoxy-) phenyl)ethynyl)dicyclopenta[de,mn] tetracene (R=H, CH_3,C_2H_5, C_3H_7); (**3**)2,7-bis (trimethylsilyl) cyclopenta[hi]aceanthrylene; (**4**) 2,8-bis(trimethylsilyl) dicyclopenta[de,mn]tetracene; (**5**) 6,12-diethynylindeno[1,2-b]fluorine; (**6**) dicyclopenta[cd,mn] pyrene; (**7**) corannulene; (**8**) dicyclopenta[hi,qr]chrysene.

The functional groups in the experimental data for molecules **1-2** are $-C_{10}H_{21}$[33]. In order to cut down on the computation time, these groups were changed to $-CH_3$. The alkyl chains are not likely to have a large effect on the electronic and optical properties of the molecules. In order to validate this claim, B3LYP and TD-B3LYP calculations were done while substituting $-C_{10}H_{21}$ with –H, $-CH_3$, $-C_2H_5$, and $-C_3H_7$. The calculations were done using the 6-311g(d,p) basis set on a neutral model. It was found that varying the alkyl chain length does not have a significant effect on the electronic and optical properties of molecules **1-2**. The ΔE_{gap} decreased by only 0.01 eV from –H to $-C_3H_7$ and the λ_{max} was redshifted by about 5 nm from –H to $-C_3H_7$. The electronic data are given in Table 1 and the absorption spectra are given in Figure 8.

Table 1. Electronic properties of 1 and 2 with varying –R groups B3LYP/6-311g(d,p)

	1			2		
-R Groups	**HOMO (eV)**	**LUMO (eV)**	**ΔE_{gap} (eV)**	**HOMO (eV)**	**LUMO (eV)**	**ΔE_{gap} (eV)**
-H	-5.19	-3.31	1.88	-5.14	-3.32	1.82
$-CH_3$	-5.18	-3.31	1.87	-5.13	-3.31	1.82
$-C_2H_5$	-5.17	-3.30	1.87	-5.12	-3.31	1.81
$-C_3H_7$	-5.17	-3.30	1.87	-5.12	-3.31	1.81

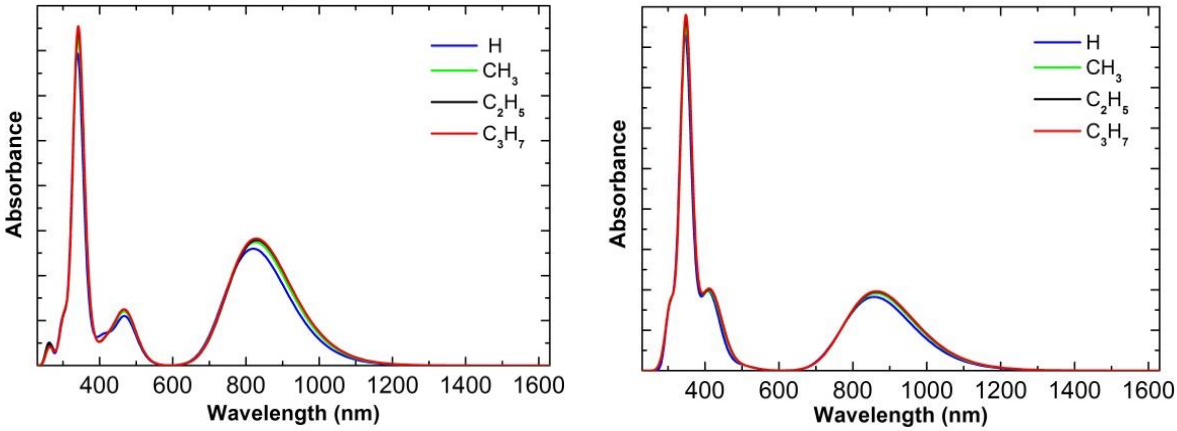

Figure 8. Predicted absorption spectra of **1**(left) and **2** (right) with varying –R groups[47]

Since the assumption that the alkyl chain functional groups do not have significant contribution to the electronic and optical properties of **1** and **2** was correct, $-CH_3$ was chosen to replace $-C_{10}H_{21}$ in all calculations of **1** and **2.** DFT calculations were done on both the neutral and anionic species of each molecule using all six functionals. The electronic data for both the conventional and improved DFT methods are given in Table 2. The data in this table are reported as the deviation in electron volts (eV) from the experimental value. For LUMO and ΔE_{gap}, the data reported first was calculated using the conventional DFT method and the data in parentheses was calculated using the improved method. Note that the HOMO for each molecule is the same for both methods since it was found from the neutral DFT calculation.

Table 2. Errors and MAEs of electronic properties of CP-PAHs

Functional	1	2	3	4	5	6	7	8	MAE
HOMO (eV)									
Experiment*	**-5.19**[33]	**-5.19**[33]	**-5.59**[33]	**-5.36**[33]	**-5.88**[42]	**-6.06**[43]	**-6.37**[43]	**-6.16**[43]	---
B3LYP	0.01	0.06	-0.15	-0.06	0.34	0.20	0.02	0.11	0.12
HSEH1PBE	0.15	0.61	0.02	0.07	0.47	0.32	0.10	0.23	0.19
CAMB3LYP	-1.24	-1.12	-1.43	-1.21	-0.81	0.32	-1.40	-1.20	1.09
PBE	0.60	0.61	0.49	0.46	0.83	0.86	0.65	0.76	0.66
TPSS	0.64	0.66	0.52	0.51	0.88	0.90	0.70	0.80	0.70
HCTH	0.53	0.55	0.42	0.41	0.76	0.80	0.59	0.70	0.60
LUMO (eV)									
Experiment*	**-3.64**[33]	**-3.62**[33]	**-3.41**[33]	**-3.45**[33]	**-4.00**[42]	**-3.48**[43]	**-2.55**[43]	**-3.35**[43]	---
B3LYP	0.33 (0.16)	0.31 (0.12)	0.34 (0.16)	0.32 (0.16)	0.52 (0.38)	0.68 (0.21)	0.55 (0.06)	0.63 (0.14)	0.46 (0.17)
HSEH1PBE	0.05 (0.27)	-0.01 (0.47)	0.05 (0.29)	0.02 (0.27)	0.24 (0.50)	0.39 (0.32)	0.28 (0.21)	0.35 (0.27)	0.17 (0.30)
CAMB3LYP	1.30 (-0.85)	1.28 (-0.81)	1.39 (-0.89)	1.35 (-0.81)	1.52 (-0.70)	1.76 (-0.80)	1.69 (-0.87)	1.74 (-0.80)	1.50 (0.82)
PBE	-0.13 (0.55)	-0.18 (0.47)	-0.24 (0.60)	-0.25 (0.52)	0.04 (0.87)	0.06 (0.61)	-0.11 (0.40)	0.01 (0.48)	0.13 (0.56)
TPSS	-0.03 (0.61)	-0.07 (0.53)	-0.12 (0.65)	-0.13 (0.58)	0.15 (0.91)	0.20 (0.66)	0.03 (0.47)	0.15 (0.55)	0.11 (0.62)
HCTH	-0.17 (0.51)	-0.22 (0.43)	-0.27 (0.57)	-0.28 (0.49)	-0.01 (0.82)	0.04 (0.57)	-0.12 (0.39)	-0.01 (0.45)	0.14 (0.53)
ΔE_{gap} (eV)									
Experiment*	**1.55**[33]	**1.57**[33]	**2.18**[33]	**1.91**[33]	**1.88**[42]	**2.58**[43]	**3.82**[43]	**2.81**[43]	---
B3LYP	0.32 (0.14)	0.25 (0.06)	0.49 (0.31)	0.38 (0.22)	0.18 (0.05)	0.48 (0.01)	0.57 (0.08)	0.52 (0.03)	0.40 (0.11)
HSEH1PBE	-0.10 (0.13)	-0.79 (-0.14)	0.06 (0.31)	-0.05 (0.20)	-0.23 (0.03)	0.07 (-0.01)	0.18 (0.11)	0.12 (0.03)	0.13 (0.11)
CAMB3LYP	2.55 (0.39)	2.40 (0.31)	2.82 (0.54)	2.56 (0.41)	2.32 (0.11)	1.43 (-1.12)	3.10 (0.53)	2.93 (0.39)	2.52 (0.47)
PBE	-0.73 (-0.04)	-0.79 (-0.14)	-0.73 (0.11)	-0.71 (0.06)	-0.79 (0.04)	-0.80 (-0.25)	-0.77 (-0.25)	-0.74 (-0.28)	0.76 (0.15)
TPSS	-0.66 (-0.02)	-0.73 (-0.12)	-0.64 (0.13)	-0.64 (0.07)	-0.73 (0.03)	-0.70 (-0.24)	-0.66 (-0.22)	-0.65 (-0.24)	0.68 (0.14)
HCTH	-0.70 (-0.02)	-0.76 (-0.12)	-0.69 (0.14)	-0.68 (0.08)	-0.77 (0.05)	-0.77 (-0.23)	-0.71 (-0.20)	-0.71 (-0.25)	0.72 (0.14)

*Note: superscripts are the references from which the data were taken.

It can be seen from the data in Table 2 that the best functional to calculate the HOMO energy level was B3LYP with an overall MAE of 0.12 eV, closely followed by HSEH1PBE with an overall MAE of 0.19 eV. Interestingly, the LUMO accuracy was only improved using the improved method for B3LYP and CAMB3LYP, which saw MAE improvements from 0.46 eV to 0.17 and 1.50 eV

to 0.82 eV respectively. However, all functionals saw improvement for ΔE_{gap} using the improved method over the conventional method. The smaller error in ΔE_{gap} for the improved method is largely due to the error cancellation of HOMO and LUMO energies[47]. B3LYP had the lowest overall MAE using the improved method, which implies that this is the best functional to use with the improved method when calculating the electronic properties of electron acceptors.

The absorption spectra were generated from TD-DFT calculations with 24 states using the conventional method for each functional and using the B3LYP/TD-CAMB3LYP method. The wavelengths of maximum absorbance peaks (λ_{max}) in nanometers (nm) were compared to the experimental values found using absorbance spectroscopy. The overlaid absorption spectra for **1** and **2** are given in Figure 9 and a summary of all λ_{max} values for each molecule is given in Table 3. The absorbance data is only given for **1-7** because experimental data could not be found for **8**. The MAEs in nm were calculated for **1-7** for each method.

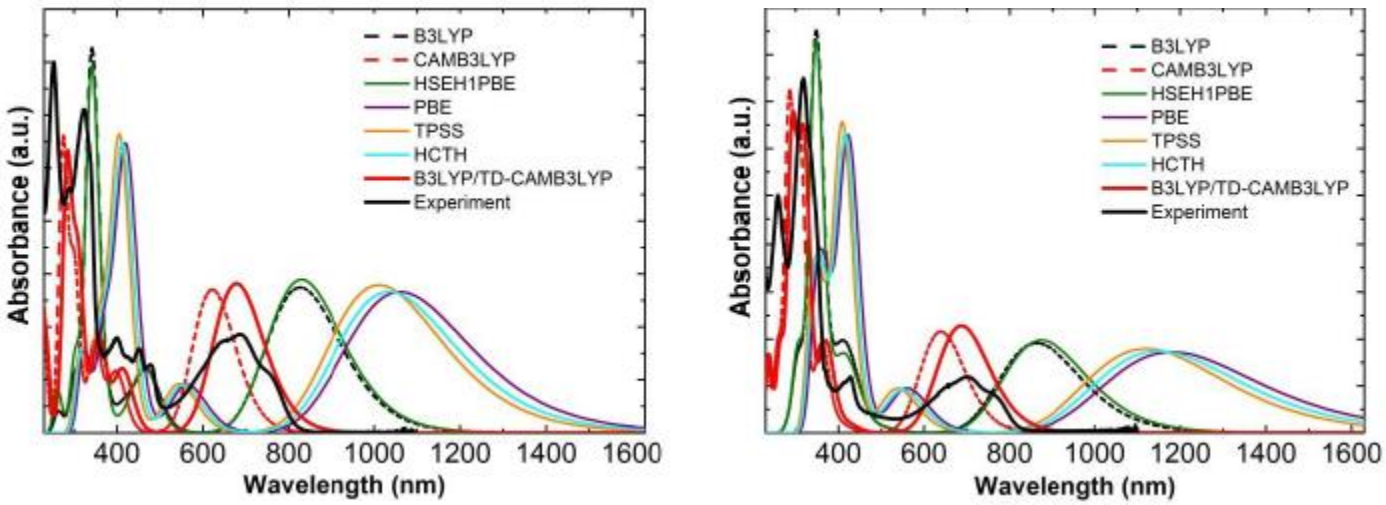

Figure 9. Absorption spectra of **1** (left) and **2** (right)[47]

Table 3. Errors and MAEs of λ_{max} (nm) for CP-PAH absorption spectra

Method	**1**	**2**	**3**	**4**	**5**	**6**	**7**	**MAE**
Experimental*	**686**[33]	**699**[33]	**548**[33]	**603**[33]	**568**[42]	**363**[44]	**286**[44-45]	---
TD-B3LYP	139	164	47	61	129	153	63	108
TD-CAMB3LYP	-65	-61	-48	-53	-21	56	23	47
TD-HSEH1PBE	142	174	39	55	118	146	56	104
TD-PBE	374	481	165	200	262	275	104	266
TD-TPSS	325	421	132	167	229	247	94	231
TD-HCTH	348	450	149	184	249	265	98	249
B3LYP/TD-CAMB3LYP	-9	-13	-25	-29	29	70	30	29

*Note: superscripts are the references from which the data were taken.

It can be seen from the data in Table 3 that the best method to generate absorption spectra was the improved method, B3LYP/TD-CAMB3LYP. This method had an overall MAE of 29 nm for the calculation of λ_{max} for **1-7.** TD-CAMB3LYP had an MAE of 47 nm. All other methods had MAEs greater than 100 nm. B3LYP/TD-CAMB3LYP is likely successful because it combines the good structural geometry provided from B3LYP with the strength of CAMB3LYP as a good functional to predict absorption spectra[47].

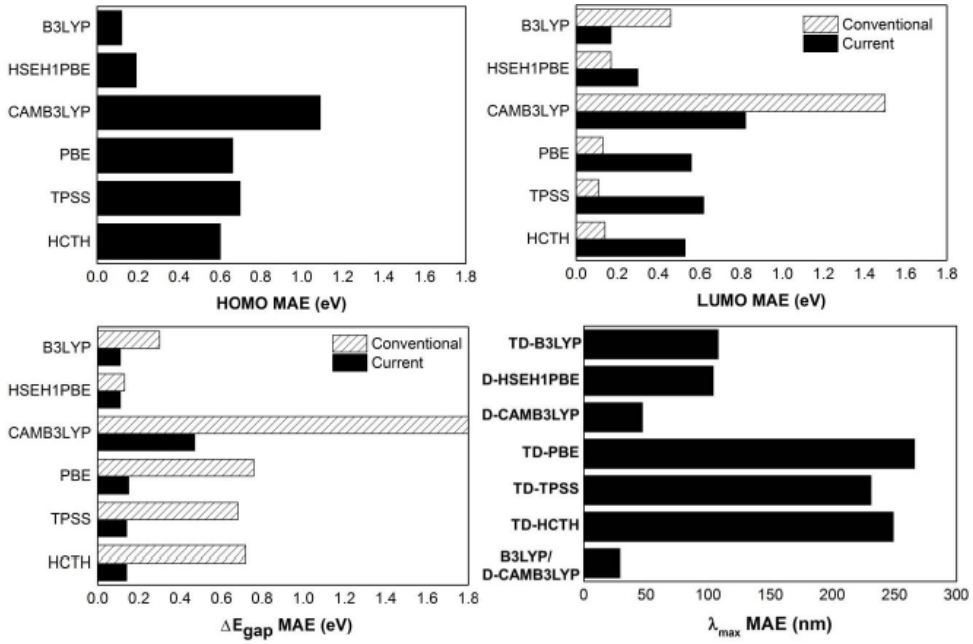

Figure 10. Mean Absolute Errors (MAEs) of predicted HOMO, LUMO, ΔE_{gap}, and λ_{max}[47]

The electronic data calculated for CP-PAHs can be used to design binary and ternary OSCs. Binary OSCs are composed of only of one type of donor molecule and one type acceptor molecule. Ternary OSCs are composed of two types of donor molecules and one type of acceptor molecule or one type of donor molecule or two types of acceptor molecules. Using the conjugated polymer P3HT as an electron donor material, five potential binary OSCs and three potential ternary OCSs have been identified. The known HOMO and LUMO energies of P3HT[33] and calculated HOMO and LUMO energies using B3LYP of **1-8** are shown in Figure 11. The dashed lines represent the HOMO and LUMO of P3HT, the black lines correspond to the HOMO and LUMO of neutral **1-8** and the red lines denote the HOMO and LUMO of anionic **1-8**.

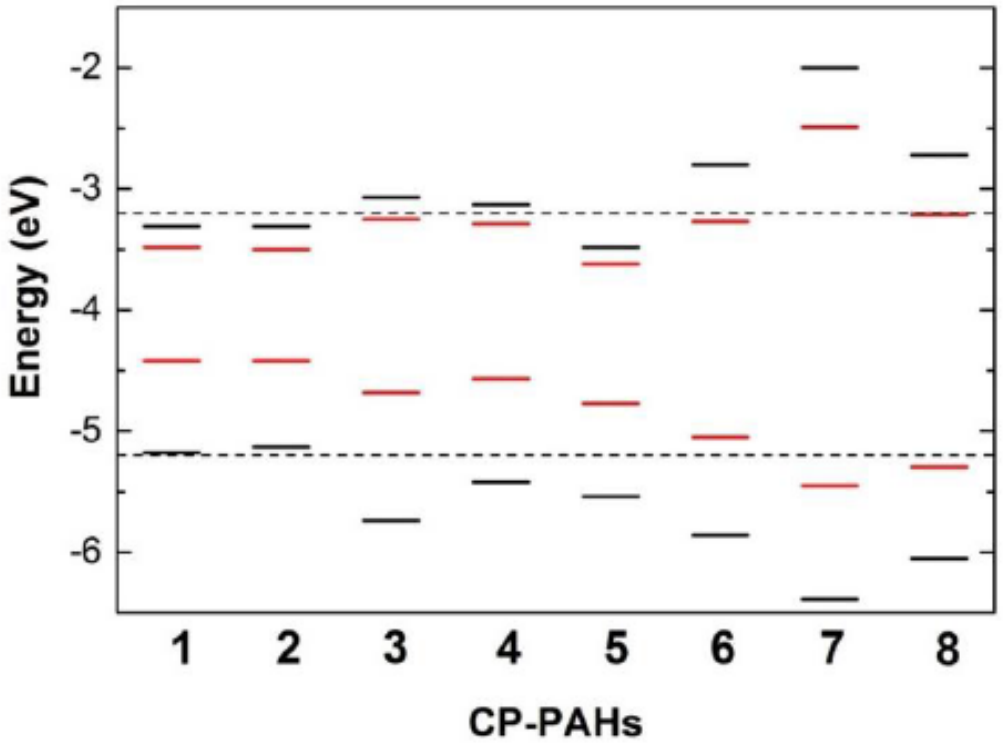

Figure 11. HOMO and LUMO energies of **1- 8** and P3HT[47]

Without considering the anionic LUMO, only **1**, **2**, and **5** can accept an electron from P3HT. However, once the anionic LUMO is considered, **1-6** all have LUMO energies lower than the LUMO of P3HT and therefore, can accept an electron from P3HT. The LUMO of **3** is about 0.2 eV lower than the LUMO of P3HT, which does not meet the ideal 0.3 eV threshold[48]. However, the remaining five CP-PAHs have LUMO energies > 0.3 eV lower than the LUMO of P3HT. Thus, these five CP-PAHs have the potential to be used as electron acceptors in binary OSCs with a P3HT donor layer.

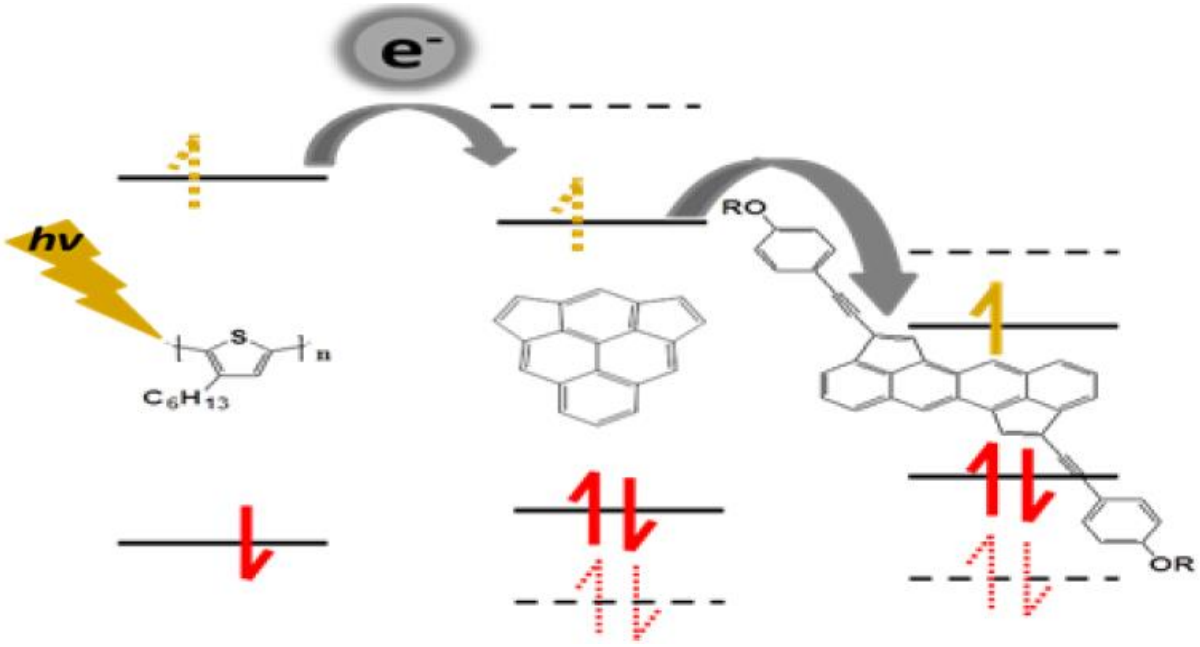

Figure 12. Ternary OSC with P3HT-**6**-**2** architecture[47]

Potential ternary OSCs with the donor-acceptor1-acceptor2 architecture have also been proposed. Ideal active layers in ternary OCSs have cascade HOMO and LUMO energy levels[47]. We have identified three potential ternary OSCs using P3HT as the donor and two CP-PAHs as acceptors. The OSCs are P3HT-**6-1**, P3HT-**6-2**, and P3HT-**6-5.** All of these have cascading HOMO and LUMO energies, making them potential designs for OCS[47]. The photoexcitation and charge transfers of ternary OSC with P3HT-**6-2** architecture is shown in Figure 12. The cascading LUMOs and HOMOs can be seen. The solid HOMO levels with the solid electrons represent the increased HOMO energy experienced when the acceptor molecules accept an electron. If the increased HOMO energies were not taken into account, the HOMO of **6** and **2** would be lower in energy than that of the P3HT. Thus, these would not be good electron acceptors for P3HT. Once the increased HOMO energies of are considered, **6** and **2** become potential electron acceptors for a ternary OSC with P3HT donor.

2.4 Electronic and optical properties of MTPA derivatives

MTPA derivatives have potential to be used as small molecule electron donors in OSCs[49]. The electronic and optical properties of a triphenyl amine based molecule, 4-vinyl-N,N-di(p-tolyl)aniline (MTPA) and six derivatives shown in Figure 13, were calculated *in-silico* and compared to experimental data. The electronic properties were calculated using the conventional method with ten density functionals: B3LYP, B3PW91, HSEH1PBE, MPW1PW91, CAMB3LYP, ωB97XD, BPV86, PBE, TPSS, and HCTH. The improved method was also utilized using the best functionals for HOMO prediction (B3LYP, B3PW91, HSEH1PBE) and the best functional for LUMO prediction (HCTH). The absorption spectra were generated from TD-DFT calculations using the convention method with all ten functionals and the improved B3LYP/TD-CAMB3LYP method. All calculations were done using the 6-31g+(d,p) basis set and dichloromethane solvent.

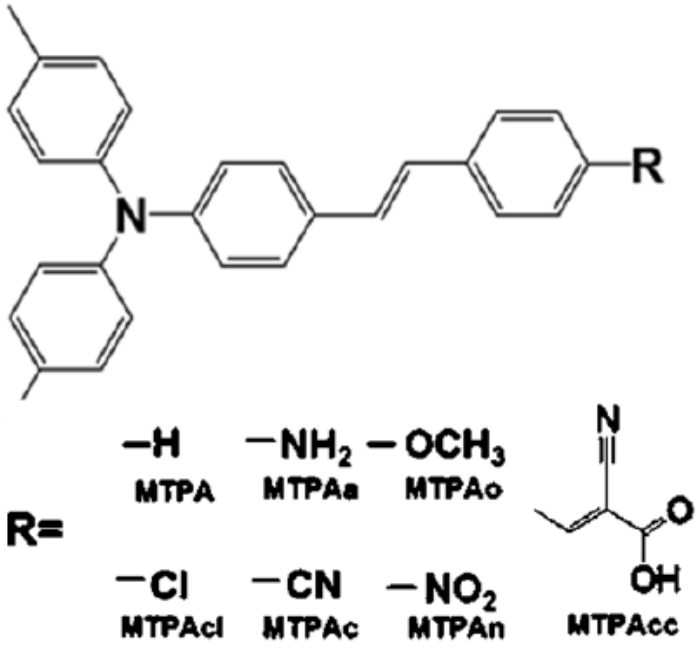

Figure 13. Structures of MTPA and derivatives[49]

Table 4. Errors and MAEs of electronic properties of MTPA derivatives

Functional	MTPAa	MTPAo	MTPA	MTPAcl	MTPAc	MTPAcc	MTPAn	MAE
HOMO (eV)								
Experiment[46]	**-5.40**	**-5.42**	**-5.54**	**-5.49**	**-5.65**	**-5.49**	**-5.54**	**---**
B3LYP[46]	0.32	0.42	0.45	0.39	0.46	0.27	0.29	0.40
B3PW91	0.39	0.37	0.39	0.33	0.40	0.21	0.24	0.34
HSEH1PBE	0.49	0.60	0.62	0.56	0.63	0.43	0.46	0.57
MPW1PW91	0.11	0.21	0.24	0.17	0.25	0.07	0.09	0.19
CAMB3LYP	-0.90	-0.80	-0.77	-0.83	-0.74	-0.90	-0.88	0.81
ωB97XD	-1.45	-1.35	-1.32	-1.39	-1.26	-1.44	-1.43	1.35
BPV86	0.85	0.96	0.98	0.91	0.97	0.72	0.75	0.90
PBE	0.93	1.04	1.06	1.00	1.05	0.80	0.84	0.99
TPSS	0.98	1.09	1.11	1.05	1.10	0.86	0.89	1.04
HCTH	0.78	0.90	0.91	0.85	0.89	0.65	0.70	0.84
LUMO (eV)								
Experiment[46]	**-2.67**	**-2.58**	**-2.77**	**-2.78**	**-3.11**	**-3.46**	**-3.46**	**---**
B3LYP[46]	1.11 (0.66)	0.95 (0.51)	0.98 (0.55)	0.92 (0.48)	0.82 (0.44)	0.46 (0.10)	0.38 (0.03)	0.80 (0.40)
B3PW91	1.06 (0.60)	0.90 (0.45)	0.93 (0.48)	0.86 (0.42)	0.76 (0.37)	0.40 (0.03)	0.39 (0.05)	0.76 (0.34)
HSEH1PBE	0.88 (0.82)	0.72 (0.68)	0.75 (0.71)	0.68 (0.65)	0.59 (0.59)	0.24 (0.25)	0.25 (0.26)	0.59 (0.57)
MPW1PW91	1.22	1.06	1.09	1.02	0.93	0.55	0.57	0.92
CAMB3LYP	2.27	2.13	2.16	2.09	1.99	1.58	1.60	1.97
WB97XD	2.84	2.46	2.74	2.66	2.46	2.14	2.22	2.50
BPV86	0.39	0.22	0.25	0.20	0.12	-0.16	-0.23	0.22
PBE	0.46	0.30	0.32	0.27	0.20	-0.08	-0.14	0.25
TPSS	0.61	0.45	0.48	0.42	0.34	-0.04	0.05	0.34
HCTH	0.39 (0.94)	0.23 (0.80)	0.25 (0.83)	0.2 0 (0.77)	0.13 (0.70)	-0.16 (0.26)	-0.19 (0.59)	0.22 (0.70)
ΔE_{gap} (eV)								
Experiment[46]	**2.73**	**2.84**	**2.78**	**2.71**	**2.54**	**2.03**	**2.08**	**---**
B3LYP[46]	0.62 (0.16)	0.53 (0.09)	0.53 (0.09)	0.53 (0.10)	0.36 (-0.02)	0.19 (-0.17)	0.09 (-0.26)	0.41 (0.13)
B3PW91	0.62 (0.16)	0.53 (0.08)	0.54 (0.09)	0.53 (0.09)	0.36 (-0.03)	0.19 (-0.17)	0.15 (-0.19)	0.42 (0.12)
HSEH1PBE	0.21 (0.15)	0.12 (0.08)	0.13 (0.08)	0.12 (0.09)	-0.04 (-0.04)	-0.19 (-0.18)	-0.21 (-0.21)	0.15 (0.12)
MPW1PW91	0.93	0.85	0.85	0.85	0.68	0.48	0.48	0.73
CAMB3LYP	3.01	2.93	2.93	2.92	2.73	2.48	2.48	2.78
WB97XD	4.13	3.81	4.06	4.05	3.72	3.58	3.65	3.86
BPV86	-0.64	-0.74	-0.73	-0.71	-0.85	-0.88	-0.98	0.79
PBE	-0.65	-0.74	-0.74	-0.73	-0.85	-0.88	-0.98	0.80
TPSS	-0.54	-0.64	-0.63	-0.63	-0.76	-0.82	-0.94	0.71
HCTH	-0.58 (-0.03)	-0.67 (-0.10)	-0.66 (-.09)	-0.65 (-0.07)	-0.76 (-0.19)	-0.81 (-0.22)	-0.89 (-0.11)	0.72 (0.12)

The HOMO, LUMO, and ΔE_{gap} data of all MTPA derivatives are given in Table 4 and are reported as the error in eV from the experimental value. The experimental and B3LYP data were obtained from reference[46]. The energies obtained using the improved method are shown in parentheses. A summary of HOMO MAE, LUMO MAE, ΔE_{gap} MAE, and overall MAE is given in Figure 14.

The top three functionals for predicting the HOMO energies were MPW1PW91, B3PW91, and B3LYP with MAEs of 0.19 eV, 0.34 eV, and 0.40 eV respectively. All other functionals had MAEs greater than 0.50 eV for the HOMO calculation. The best three functionals for predicting LUMO energies were HCTH, BPV86, and PBE with MAEs of 0.22 eV, 0.22 eV, and 0.25 eV respectively. Even the LUMO values calculated using the improved method had MAEs greater than 0.3 eV. Interestingly, the LUMO prediction accuracy of all functionals except BPV86 and HCTH, using both the conventional and improved methods increased as the electron withdrawing ability of the functional group increased.

The smallest MAEs for ΔE_{gap} were calculated using the improved method. The best functional using the conventional method was HSEH1PBE, which had an MAE of 0.15 eV. The MAEs of B3PW91, HSEH1PBE, HCTH, and B3LYP with the improved method were 0.12 eV, 0.12 eV, 0.12 eV, and 0.13 eV respectively. All four functionals used with the improved method calculated ΔE_{gap} more accurately than any other functional using the conventional method. This result indicates the importance of considering the anionic LUMO when calculating ΔE_{gap}.

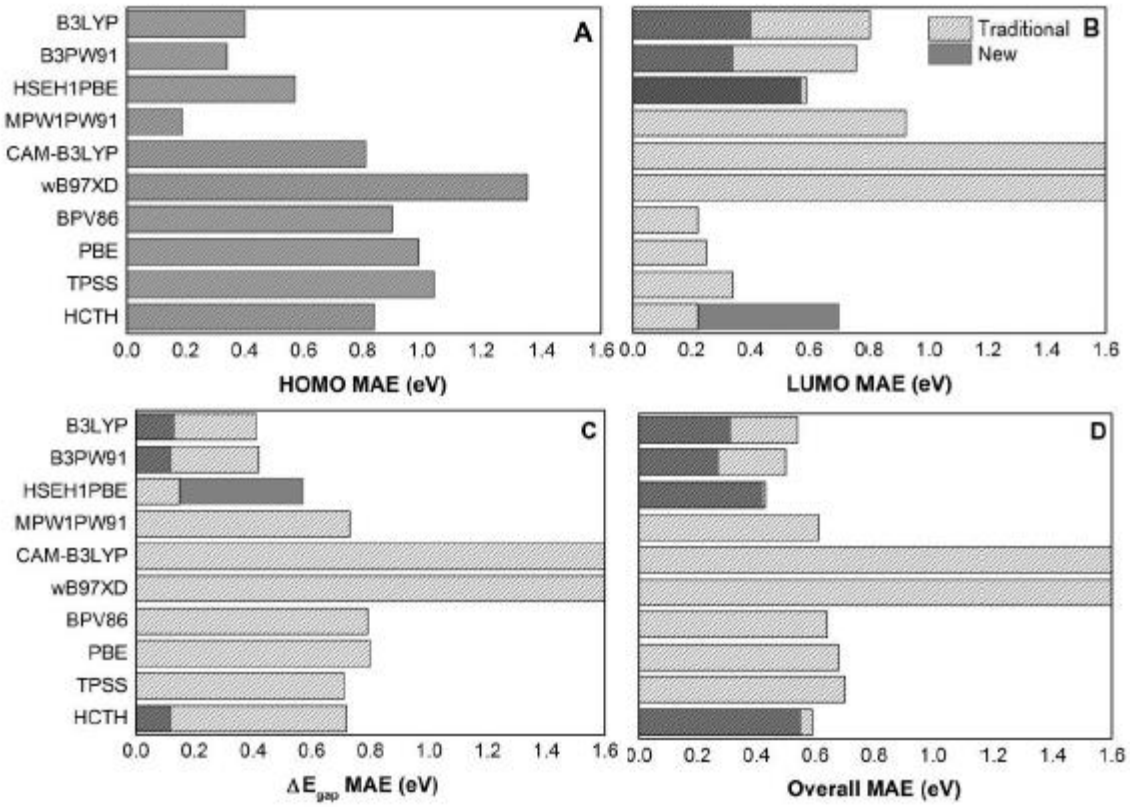

Figure 14. MAEs for calculated electronic properties of MTPA and derivatives[49]
A) HOMO MAE **B**) LUMO MAE **C**) ΔE_{gap} MAE **D**) Average MAE of HOMO, LUMO, ΔE_{gap}

The absorption spectra were generated from TD-DFT calculations with 12 states using the conventional method for each functional and using the B3LYP/TD-CAMB3LYP method. The wavelengths of maximum absorbance peaks (λ_{max}) in nanometers (nm) were compared to the experimental values found using absorbance spectroscopy. The overlaid absorption spectra for all MTPA derivatives are given in Figure 15. A summary of all λ_{max} values for each molecule is given in Table 5 and reported as the error from the experimental value in nm.

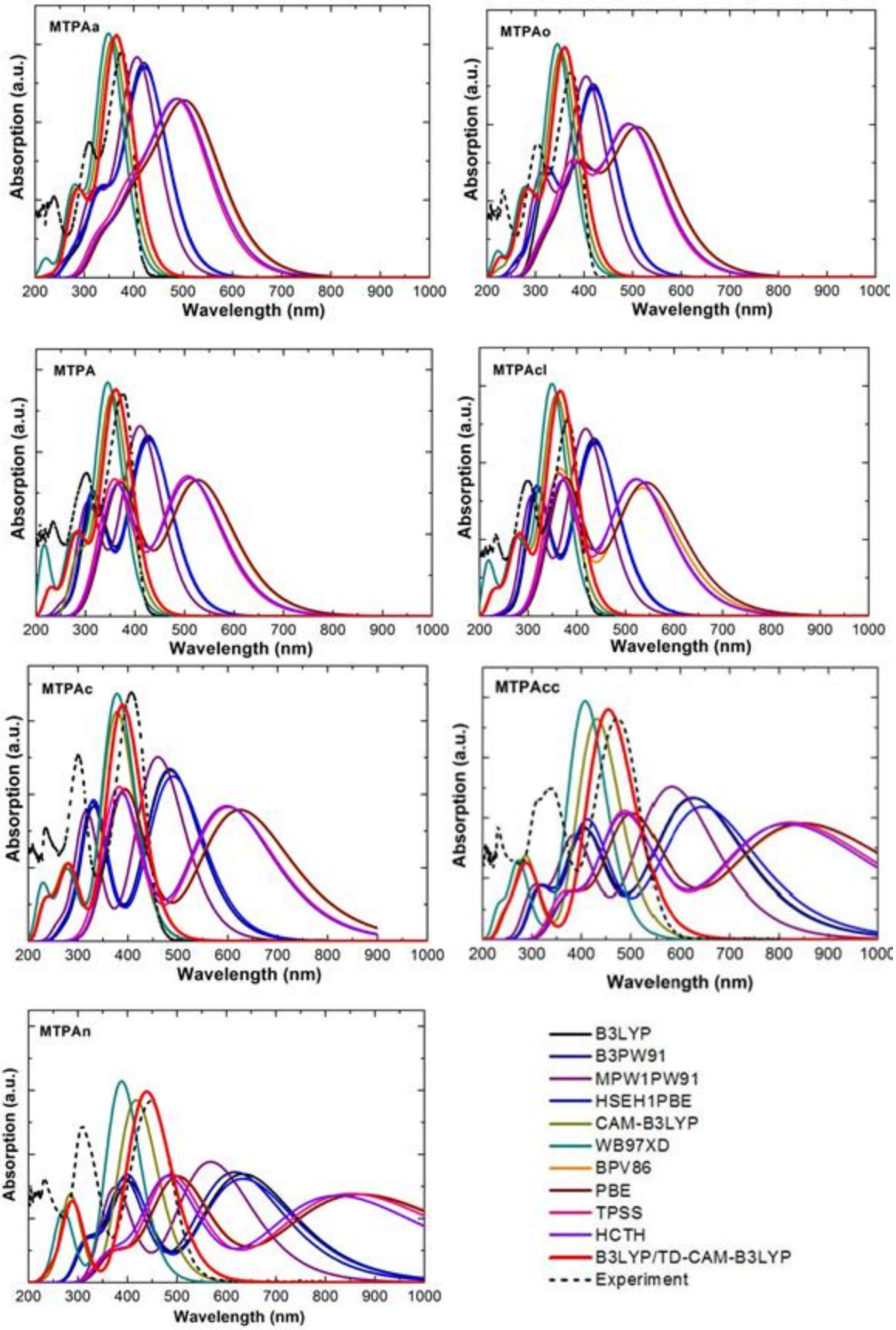

Figure 15. Absorption spectra of MTPA and derivatives[49]

Table 5. Errors and MAEs of λ_{max} (nm) for MTPA absorption spectra

Functional	MTPAa	MTPAo	MTPA	MTPAcl	MTPAc	MTPAcc	MTPAn	MAE
Experiment[46]	**375**	**375**	**375**	**380**	**407**	**472**	**448**	---
TD-B3LYP[46]	48	47	53	57	78	156	186	89
TD-B3PW91	47	45	52	56	77	153	169	86
TD-HSEH1PBE	48	46	54	58	83	174	186	93
TD-MPW1PW91	33	30	35	39	53	110	120	60
TD-CAMB3LYP	-18	-22	-21	-22	-29	-40	-30	26
TD-WB97XD	-26	-29	-30	-31	-29	-64	-60	38
TD-BPV86	135	137	152	155	225	380	426	230
TD-PBE	137	139	154	163	218	378	422	230
TD-TPSS	118	119	133	143	194	352	405	209
TD-HCTH	123	123	137	145	191	342	387	207
B3LYP/TD-CAMB3LYP	-10	-14	-13	-13	-18	-17	-9	13

It can be seen from the data in Table 5 that the best method to generate absorption spectra for MTPA and derivatives was the improved method, B3LYP/TD-CAMB3LYP. This method had an overall MAE of 13 nm for the calculation of λ_{max} of all seven MTPA molecules**.** TD-CAMB3LYP and TD-WB97XD were reasonably accurate with MAEs of 26 nm and 38 nm respectively. All other TD-DFT methods had MAEs greater than 60 nm. This result further validates the use of the B3LYP/TD-CAMB3LYP method to predict absorption spectra.

As was observed in the calculations of the electronic properties of MTPA derivatives, the MTPA functional group had an effect on the accuracy of the TD-DFT method. When calculating the electronic properties, the accuracy of the method generally increased as the functional group became more electron withdrawing. However, it can be seen in Table 5 that the accuracy of every method decreased as the functional group became more electron withdrawing. This decrease in accuracy is likely due to the decrease in spatial overlap between the virtual and occupied orbitals as the electron withdrawing ability of the functional group increases[46]. TD-CAMB3LYP, TD-WB97XD, and B3LYP/TD-CAMB3LYP underestimated λ_{max} as the electron

withdrawing ability of the functional group increased. All other methods saw an overestimation in λ_{max} as the functional group was substituted from electron donating ($-NH_2$) to electron withdrawing ($-NO_2$).

We have demonstrated that the functional group present in an MTPA derivative significantly affects the accuracy of DFT and TD-DFT calculations to predict the electronic and optical properties. A general trend was observed for most functionals with the conventional and improved methods that as the electron withdrawing ability of the functional group increases, the accuracy of the functional to predict the electronic properties also increases. The opposite trend was observed when using TD-DFT calculations to generate the absorption spectra of MTPA derivatives. It was observed for all TD-DFT methods that as the electron withdrawing ability of the functional group increased, the accuracy of the TD-DFT method decreased. Therefore, when performing DFT and TD-DFT calculations, one should be aware of the electron withdrawing ability of the functional groups present and consider the changes in calculation accuracy associated with the electron withdrawing ability of the functional groups. Figure 16 illustrates these general trends in calculation accuracy for the functional groups present in the MTPA derivatives studied.

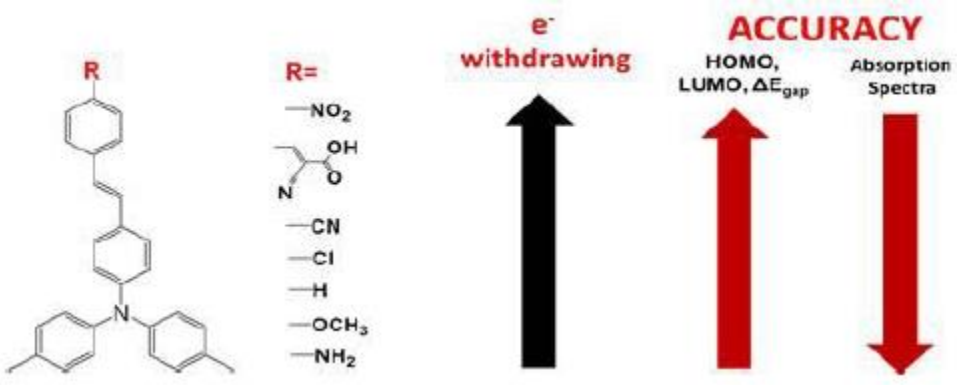

Figure 16. Trends in accuracy with various –R groups[49]

CHAPTER 3
COAL DYE-SENSITIZED SOLAR CELLS

3.1 Coal as a sensitizer

Coal is a sedimentary organic rock that is a conglomeration of prehistoric vegetation that has been subjected to intense heat and pressure for millions of years. It is mainly composed of carbon, hydrogen, and oxygen[50]. Other elements such as sulfur, nitrogen, aluminum, and zirconium may also be present[51]. There are four types of coal: lignite, sub-bituminous, bituminous, and anthracite. The type of coal that is formed depends how long the vegetation is exposed to intense heat and pressure. The degree of alteration from least mature to most mature is lignite < sub-bituminous < bituminous < anthracite. The different types of coal vary in color and hardness, as well as chemical identity[52]. The type of coal found in Illinois is bituminous and it typically has a high sulfur content[53]. Illinois bituminous coal was used in this study.

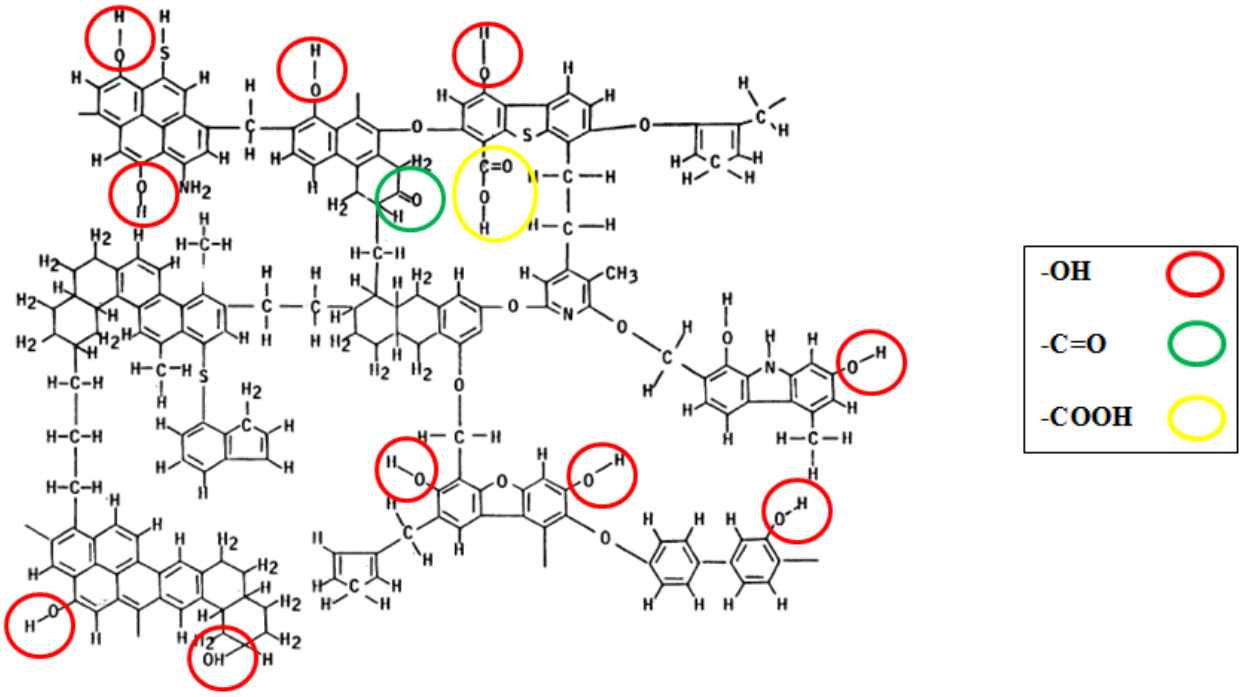

Figure 17. Proposed structure of bituminous coal. Adapted from ref.[52]

Since coal is combination of many compounds, it does not have a definite structure. A proposed structure of bituminous coal is shown in Figure 17. It can be seen that coal contains many aromatic compounds. These aromatic compounds are in similar structure to known photosensitizers used in OSCs and DSSCs[20-21, 24, 26, 35]. This proposed structure of coal contains twelve anchoring groups, which are needed for dye molecules in DSSCs. The anchoring groups in this coal structure are hydroxyl (red), carbonyl (green), and carboxylic acid (yellow).

Coal's structural similarities to known OSC and DSSC photosensitizers give it the potential to be used as a photosensitizer in these devices. Another attractive photosensitizer property of coal is that its black color allows it to absorb light at many wavelengths. Coal is also cheap and abundant[50] compared to expensive ruthenium dyes that have been used in DSSC[20]. Additionally, using coal in solar cells to generate electricity would be a much better application for coal compared to burning it to produce electricity.

3.2 Coal dye solutions

In this study, coal solutions were prepared by subjecting coal powder to various organic solvents. DSSCs were made using the coal solutions as dyes to stain a TiO_2 layer on SnO_2 coated conductive glass. Additional dye solutions were prepared using oxidized coal powder and the same organic solvents. Oxidized coal powder was prepared by subjecting coal powder to strong oxidizing agents in an attempt to add additional anchoring groups. Size controlled coal dye solutions were also prepared by filtering the coal dye solutions with 100 nm syringe filters.

Coal powder was made by grinding a small piece (~1 gram) of Southern Illinois bituminous coal using a mortar and pestle for about 10 minutes. This resulted in a very fine

powder in which one could not visibly tell the different between grains. 50 grams of coal powder was made initially and was used throughout the duration of the study.

$KMnO_4$ oxidized coal powder was made by adding 5 grams of coal powered to 1.50 grams $KMnO_4$ in 100 mL of DI water. The solution was stirred for 24 hours and the solid was collected by vacuum filtration. The solid coal was washed with DI water to remove excess $KMnO_4$ until the filtrate was clear. The solid was then allowed to air dry for 3 days. H_2O_2 oxidized coal was made by adding 7 grams of coal powder to 100 mL of 15% H_2O_2. The solution was stirred for 24 hours and the solid was collected by vacuum filtration. The solid was washed with DI water and allowed to air dry for 3 days. FT-IR spectroscopy was done on the solid coal powders. The spectra were identical in peak wavenumber, indicating that no new functional groups were adding during oxidation. However, this does not mean that additional functional groups of the same type were not added.

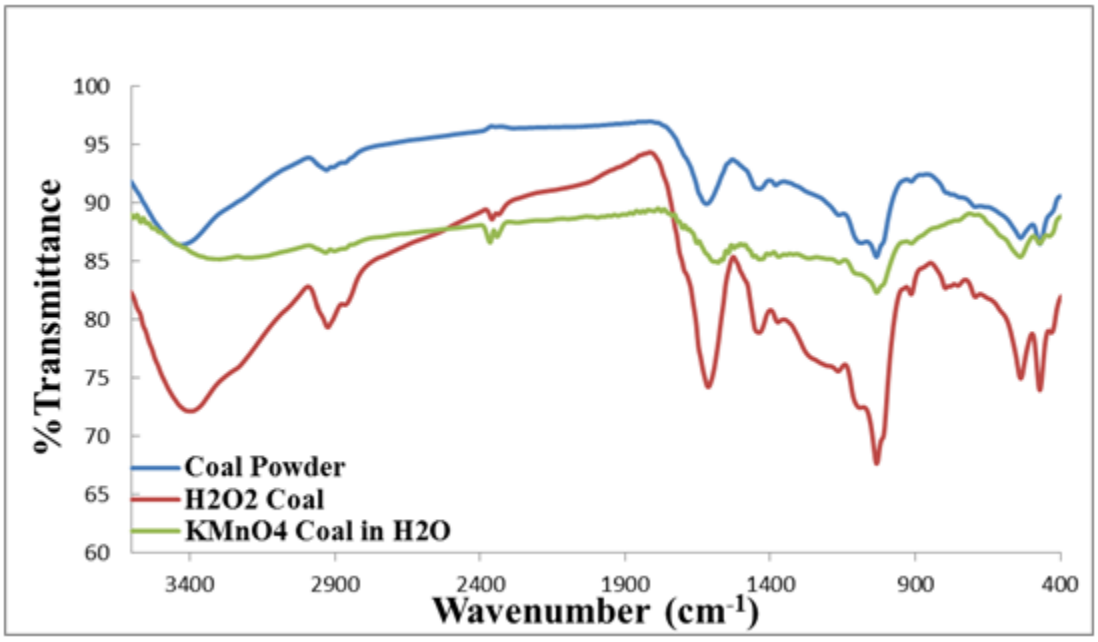

Figure 18. Overlaid FT-IR spectra of solid coal powders

Coal dye solutions were prepared by adding 3.0 g of coal powder (oxidized or unoxidized) to 30 mL of solvent. The solvents studied were tetrahydrofuran (THF), mesityl oxide, and cyclohexanone. An additional coal dye solution was prepared by mixing 10 mL of each solvent and is referred to in this study as mixed solvent or cocktail coal dye. The coal dye solutions were prepared in 50 mL disposable plastic test tubes with screw-on lids. After combining the coal powder and solvents, the solutions were shaken vigorously and allowed to equilibrate for 3 days. After 3 days, the resulting colored liquids were removed by carefully pipetting the solution at the top. These solutions did not contain any visible coal and were stored in glass vials. Instead of pipetting, the size controlled dyes were filtered using 100 nm syringe filters. The color of the solution varied between solvents and the type of coal powder used. THF gave the darkest dye using unoxidized coal powder, and the dyes made from H_2O_2 oxidized coal were much darker in color than the dyes made using unoxidized coal. The mixed solvent dye yielded a solution that was darker than the three parent solutions individually. The darker colored dyes likely contain more dissolved coal than the lighter colored coal dyes. Thus, one would expect that the darker dyes will add more coal to the TiO_2 layer during the staining process.

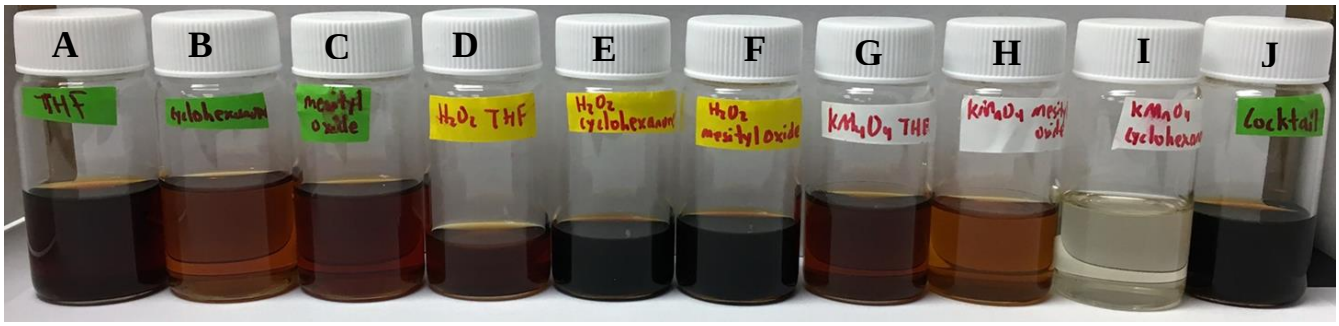

Figure 19. Coal dye solutions after pipetting **A)** coal/tetrahydrofuran **B)** coal/cyclohexanone **C)** coal/mesityl oxide **D)** H_2O_2 oxidized coal/tetrahydrofuran **E)**H_2O_2 oxidized coal/cyclohexanone **F)** H_2O_2 oxidized coal/mesityl oxide **G)** $KMnO_4$ oxidized coal/tetrahydrofuran **H)** $KMnO_4$ oxidized coal/mesityl oxide **I)** $KMnO_4$ oxidized coal/cyclohexanone **J)** coal/mixed solvent

3.3 Coal solar cell fabrication

Excluding the coal dye solutions, all solar cells were fabricated using materials purchased from the Institute for Chemical Education at the University of Wisconsin as part of the Nanocrystalline Solar Cell Kit. The kit included Degussa P25 colloidal TiO_2, iodide/tri-iodide electrolyte in ethylene glycol solution, SnO_2 coated conductive glass slides (1" x 1"), copper tape, and woodless soft graphite pencil[34]. The provided procedure was used, but was slightly adapted for this study.

The TiO_2 layer was made by spreading TiO_2 slurry onto the conductive side of SnO_2 coated conductive glass. The TiO_2 slurry was prepared by grinding 6 grams of colloidal TiO_2 with 12 mL of pH 3.5 nitric acid with a mortar and pestle. The acid was added in 2 mL aliquots while grinding over the course of 30 minutes. The slurry was allowed to sit for 30 minutes for before spreading. The conductive side of SnO_2 coated conductive glass slides were washed with ethanol and transparent tape was applied to three sides in order to control the thickness of the TiO_2 layer. A small amount of TiO_2 slurry was placed in a line near the top piece of tape using a spatula. The TiO_2 slurry was spread using the narrow side of a glass microscope slide. The tape was removed and the TiO_2 coated slides were annealed at 450 ^oC for 45 minutes in an aluminum foil oven using a heat gun.

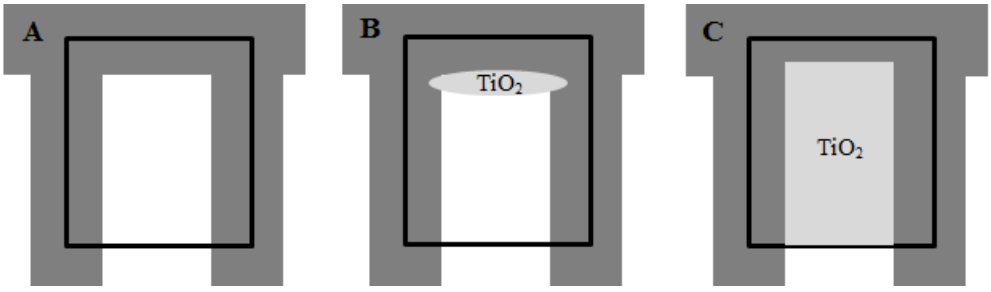

Figure 20. Diagram of preparing the TiO_2 layer A) Conductive glass slide with tape B) TiO_2 slurry applied to conductive glass C) TiO_2 slurry spread on conductive glass

DSSC active layers were prepared by staining the annealed TiO_2 conductive glass slides with the coal dye solutions. Two annealed TiO_2 conductive glass slides were stained for each coal dye solution. 20 mL of each coal dye solution was added to a glass petri dish with a glass cover. Two annealed TiO_2 slides were placed face down into each dye solution and stained simultaneously. The annealed TiO_2 slides were stained for 24 hours. After staining, the slides were removed and carefully washed with ethanol. The slides were stored in covered petri dishes until all active layers were prepared. An additional type of DSSC active layer was prepared by adding 0.5 grams of coal powder directly to the TiO_2 slurry and following the same procedure to prepare the blank annealed TiO_2 slides. Monolayer OSC active layers were made by applying coal dye solutions directly to the conductive side of SnO_2 coated glass and evaporating the solvent. The solvent was quickly evaporated by adding coal dye solution dropwise to SnO_2 coated glass while heating on a hot plate. Approximately 1-2 mL of coal dye solution was evaporated for each OSC active layer. Coal/THF, coal/mesityl oxide, and coal/cyclohexanone were used as the coal dye solutions for OSCs.

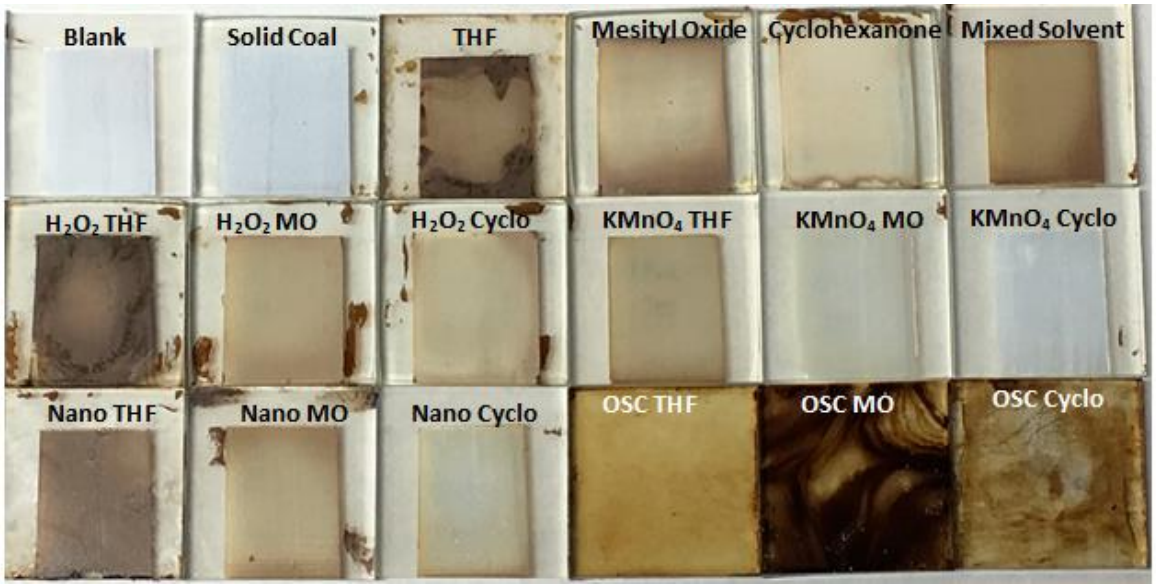

Figure 21. Coal solar cell active layers

Carbon coated counter electrodes were used in all coal solar cells. These were prepared by adding a graphite layer to the conductive side of SnO_2 coated glass. The glass was first cleaned with ethanol. The graphite layer was added by lightly drawing in the same direction on the conductive glass surface with a woodless soft graphite pencil.

All solar cells were assembled by placing a single drop of iodide/tri-iodide electrolyte in the center of the carbon counter electrode and immediately placing the solar cell active layer face down on top of the carbon counter electrode. The DSSC active layer electrodes were carefully added so that the entire stained TiO_2 layer was in contact with the carbon layer; only the glass that was protected using tape was left exposed. Binder clips were applied to the sides on the solar cells in order to keep the anode and cathode in place. The excess electrolyte was wiped from the edges using a Kimwipe. A small piece of copper tape was applied to both exposed glass edges. The solar cells were placed active layer face down and allowed to equilibrate for 1 hour before testing.

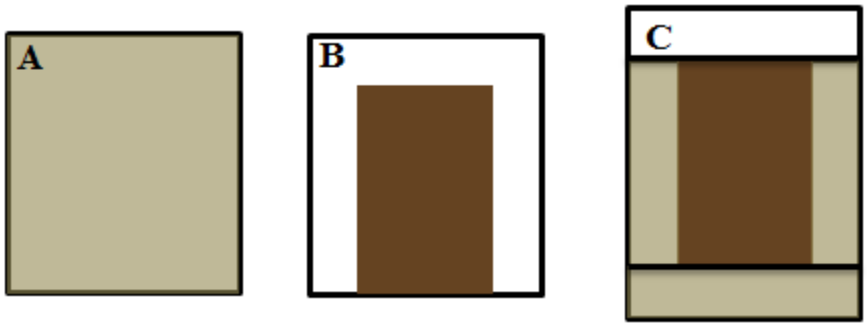

Figure 22. Diagram of DSSC assembly A) Graphite carbon electrode B) Stained TiO_2 electrode C) Electrodes sandwiched together with exposed ends

3.4 Electrical output of coal solar cells

The electrical output of coal solar cells was measured under ~1,500 W/m^2 irradiance from a 150 W incandescent light source. All measurements were made with the solar cell active layer face up. The open circuit voltage (V_{oc}) and short circuit current (I_{sc}) were measured with a single multimeter with alligator clamp leads. Current-voltage curve (IV curve) data was obtained by placing two multimeters in series with a 500 Ω potentiometer and the solar cell. The resistance was varied over the course of about 10 seconds.

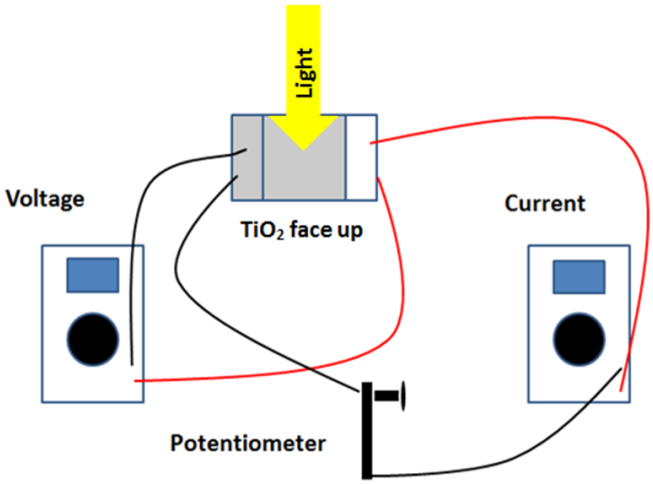

Figure 23. Multimeter setup used to generate IV curves

Slow motion video was used to capture the current and voltage responses due to the change in resistance. The data from the slow motion video was transferred to an Excel spreadsheet and the maximum power output (P_{max}) of each solar cell was identified. IV curves were plotted using only the V_{oc}, I_{sc}, and $P_{max.}$ The IV curves of each solar cell made using the original coal dye solutions compared to its altered versions are shown in Figures 24-26. The top five IV curves are shown in Figure 27.

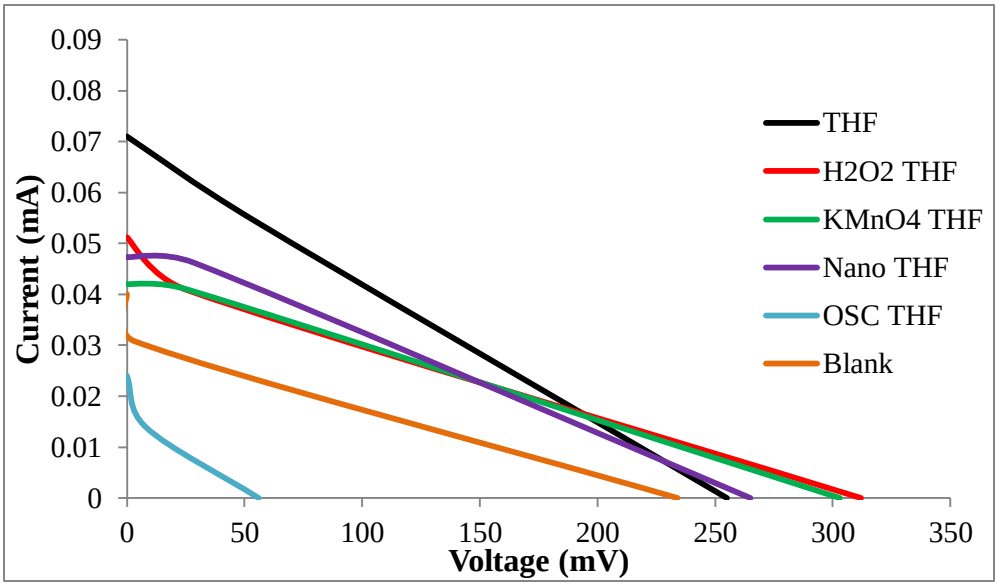

Figure 24. IV curve of THF coal solar cells

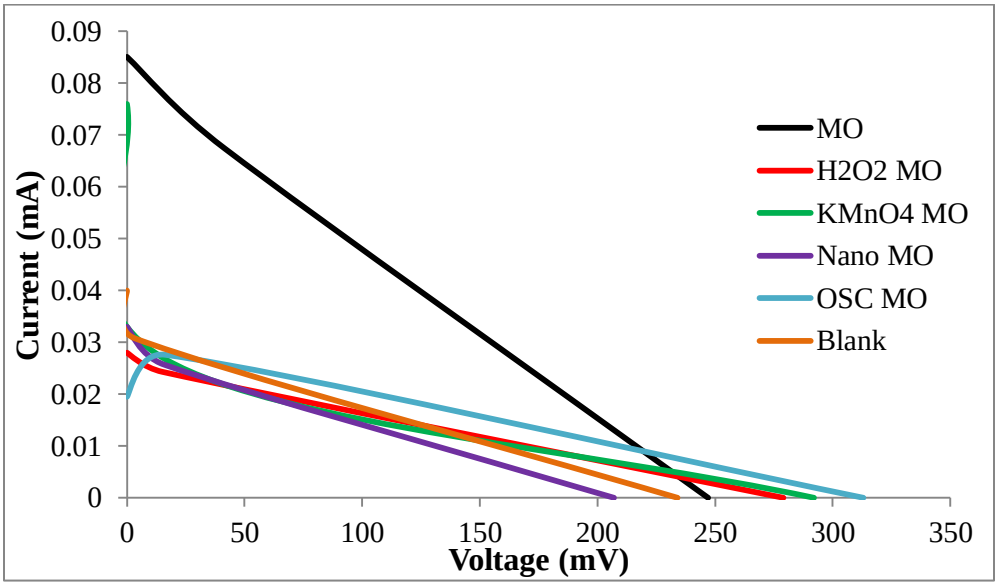

Figure 25. IV curve of mesityl oxide coal solar cells

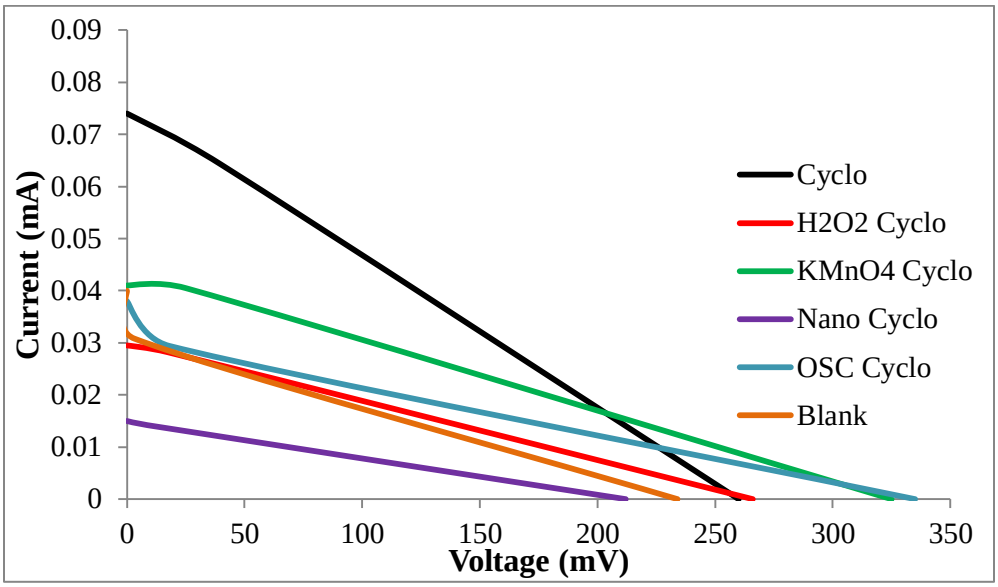

Figure 26. IV curve of cyclohexanone coal solar cells

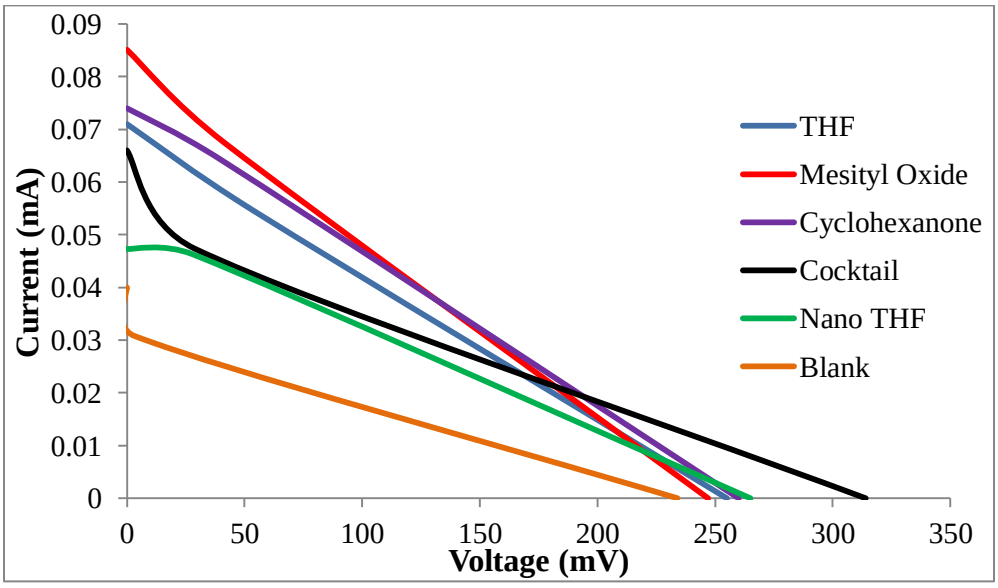

Figure 27. IV curves of five best coal solar cells

Interestingly, the best coal solar cells were DSSCs made using unaltered coal dye solutions. The next best coal solar cell had an active layer made using the mixed solvent coal dye solution. The mixed solvent coal DSSC had a higher V_{oc} than the parent coal dye solution DSSCs, but had a lower I_{sc}. The nano THF coal DSSC had lower V_{oc}, I_{sc}, and P_{max} compared to the other top coal DSSCs, but its IV curve had the highest fill factor. This indicates that using nano sized coal particles may give a more uniform active layer. Moreover, coal solar cells have significantly higher electrical outputs compared to the blank. It has been shown that coal solutions can be utilized as dye photosensitizers to make functioning DSSCs and OSCs.

IV curve diagrams are useful to quickly compare the electrical outputs of solar cells. However, the IV curves in Figures 24-27 provide a more qualitative way to compare the devices because the active area of the device is not considered. In order to further compare the coal solar cells, the efficiency (η) of each solar cell was calculated using the formula in Equation 2 from reference[54]. The active layer area of each individual solar cell was measured. The DSSC active layer was assumed to be the entire stained TiO_2 layer and was measured before device fabrication. The OSC active layer area was measured after fabrication; the area that was not blocked by binder clips was considered to be the active layer.

$$\eta = \frac{\max power\ (W)}{active\ layer\ area\ (m^2) \times irradiance\ (\frac{W}{m^2})} \times 100\% = \frac{P_{max}}{A \times E_e} \times 100\% \qquad (2)$$

Table 6. Electrical output of coal solar cells

Solar Cell	V_{oc} (mV)	I_{sc} (mA)	P_{max} (μW)	Efficiency (10^{-4} %)
Mesityl Oxide	247	0.0851	2.80	5.66
Cyclohexanone	260	0.074	2.55	4.50
THF	255	0.071	1.82	4.41
Mixed Solvent	314	0.066	1.38	3.22
Nano THF	265	0.0473	1.32	3.19
$KMnO_4$ THF	303	0.042	1.04	2.44
H_2O_2 THF	312	0.0512	1.03	2.35
$KMnO_4$ Cyclohexanone	325	0.041	1.01	2.31
H_2O_2 Cyclohexanone	266	0.0295	0.48	1.07
OSC Cyclohexanone	335	0.038	0.53	0.99
Nano Mesityl Oxide	207	0.033	0.41	0.97
$KMnO_4$ Mesityl Oxide	292	0.076	0.44	0.89
OSC Mesityl Oxide	313	0.0195	0.45	0.81
H_2O_2 Mesityl Oxide	279	0.028	0.37	0.78
Solid Coal	284	0.0218	0.15	0.33
Nano Cyclohexanone	212	0.015	0.12	0.30
Blank	234	0.04	0.09	0.23
OSC THF	56	0.024	0.11	0.20

The solar cells in Table 6 are listed from most efficient to least efficient. It can be seen that the majority of coal solar cells were significantly more efficient than the blank and therefore are better solar cells. The best coal solar cell, a DSSC made using mesityl oxide coal dye solution, is nearly 25 times as efficient as the blank! It is should also be noted that a solar cell with higher maximum power compared to another solar cell does not necessarily mean that it is more efficient. For example, OSC Cyclohexanone has a higher maximum power point compared to H_2O_2 Cyclohexanone. However, OSC Cyclohexanone is less efficient because it has a larger active area. There are many possibilities for error when assembling and testing devices. Therefore, the coal solar cells below the red dotted line in Table 6 are not considered significantly different from the blank. This leaves 14 out of 17 coal solar cells that are significantly different in electrical output compared to the blank. This farther demonstrates the potential for coal as photosensitizer in DSSCs and OCSs.

Although the solvent used to prepare the coal dyes is removed after staining the TiO_2 layer, the choice of solvent for coal dyes may have an effect on the overall efficiency of coal DSSCs. One would assume that darker colored coal dye solutions contain more dissolved coal. THF coal dye is significantly darker than both mesityl oxide and cyclohexanone coal dyes, indicating that it contains more dissolved coal. The TiO_2 layer stained using THF coal dye was significantly darker than TiO_2 layers stained with mesityl oxide and cyclohexanone coal dyes. However, the TiO_2 layers stained using mesityl oxide and cyclohexanone coal dyes appeared to be more uniform than the TiO_2 layer stained with THF coal dye. The TiO_2 layer stained with THF coal dye had random spots of deposited coal. The spots are likely caused by THF evaporating and depositing unequal amount of coal on the TiO_2 surface. The uneven coal layer may be responsible for the lower efficiency of THF coal solar cells compared to mesityl oxide and cyclohexanone coal solar cells. Therefore, nonvolatile solvents may be the better solvent choice to prepare coal dye solutions for coal DSSCs.

CHAPTER 4
CONCLUSIONS AND FUTURE STUDIES

4.1 Conclusions

An improved DFT method that better represents experimental cyclic voltammetry was developed to predict the electronic properties of CP-PAHs and MPTA derivatives. This method uses the HOMO from the neutral molecule and the LUMO from anionic molecule to calculate $\Delta E_{gap.}$ This method more accurately predicted the LUMO of CP-PAHs when using the B3LYP and CAMB3LYP functionals and more accurately predicted the LUMO of MTPA derivatives when using the B3LYP, B3PW91, and CAMB3LYP functionals. Furthermore, ΔE_{gap} prediction was improved using the improved method compared to the conventional method for all functionals studied. An improved TD-DFT method was also utilized to predict the absorption spectra of CP-PAHs and MPTA derivatives. This method employed a TD-CAMB3LYP calculation on a structure optimized using B3LYP. This improved B3LYP/TD-CAMB3LYP method had the smallest MAE in the study of CP-PAHs and MTPA derivatives.

Monolayer organic solar cells and dye-sensitized semiconductor solar cells were fabricated using coal dye solutions as photosensitizers. Although a number of variables were changed to yield different coal dye solutions, the best solar cells were made using the original solvents. The majority of coal solar cells had significantly more electrical output compared to the blank. Thus, we have shown that OSCs and DSSCs can be assembled using coal dye solutions as photosensitizers.

4.2 Future studies

The ability to predict the electronic and absorption spectra of electron acceptors and donors is crucial for the development of solar cells. The improved computational methods used in our study of CP-PAHs and MTPA derivatives should be applied to study other electron acceptors and donors. The electronic data found using the improved methods to study other electron acceptors and donors may allow for the design of potential OSCs that would not have been identified using the conventional methods.

Although it was shown that coal dye solutions can be used as photosensitizers in OSCs and DSSCs, there is much room to improve these devices. The highest efficiency coal solar cell was a DSSC made with coal mesityl oxide dye solution. This solar cell was only 0.00566 % in efficiency. It is possible that coal solar cells may absorb light closer to the UV region, and the incandescent light source may emit low UV intensity. Using a light source that more resembles the solar spectrum may make coal solar cells more efficient. Better coal DSSCs may also be prepared if preprinted TiO_2 slides were used instead of preparing TiO_2 slides by hand. Also, since coal has a proposed structure to electron acceptors, it would be an interesting future study to assemble binary organic solar cells using coal dye solutions as an electron acceptor with a known donor molecule such as P3HT.

REFERENCES

1. Shafiee, S.; Topal, E., When will fossil fuel reserves be diminished? *Energy policy* **2009,** *37* (1), 181-189.

2. Agency, I. E., Key World Energy Statistics 2015.

3. Smalley, R. E., Future Global Energy Prosperity: The Terawatt Challenge. *Mrs Bulletin* **2005,** *30* (06), 412-417.

4. Zweibel, K., *The terawatt challenge for thin-film PV*. National Renewable Energy Laboratory: 2005.

5. American Chemical Society, A. G. U., et. al. *Statement on climate change from 18 scientific associations*; 2009.

6. Seeley, J. T.; Romps, D. M., The effect of global warming on severe thunderstorms in the United States. *Journal of Climate* **2015,** *28* (6), 2443-2458.

7. Zhang, K.; Douglas, B. C.; Leatherman, S. P., Global warming and coastal erosion. *Climatic Change* **2004,** *64* (1-2), 41-58.

8. Dai, A., Increasing drought under global warming in observations and models. *Nature Climate Change* **2013,** *3* (1), 52-58.

9. Haarsma, R. J.; Hazeleger, W.; Severijns, C.; Vries, H.; Sterl, A.; Bintanja, R.; Oldenborgh, G. J.; Brink, H. W., More hurricanes to hit western Europe due to global warming. *Geophysical Research Letters* **2013,** *40* (9), 1783-1788.

10. McMichael, A. J.; Woodruff, R. E.; Hales, S., Climate change and human health: present and future risks. *The Lancet* **2006,** *367* (9513), 859-869.

11. Crabtree, G. W.; Lewis, N. S., Solar energy conversion. *Physics today* **2007,** *60* (3), 37-42.

12. Vesborg, P. C.; Jaramillo, T. F., Addressing the terawatt challenge: scalability in the supply of chemical elements for renewable energy. *RSC Advances* **2012,** *2* (21), 7933-7947.

13. Ottinger, R. L., Biofuels-Potential, Problems & (and) Solutions. *Fordham Envtl. L. Rev.* **2009,** *19*, 253.

14. Acton, Q. A., *Solar Cells—Advances in Research and Application: 2013 Edition*. ScholarlyEditions: 2013.

15. Administration, U. S. E. I., How many nuclear power plants are in the United States, and where are they located? 2016.

16. Institute, N. E., Nuclear Energy Around the World. 2015.

17. Armaroli, N.; Balzani, V., The future of energy supply: challenges and opportunities. *Angewandte Chemie International Edition* **2007,** *46* (1-2), 52-66.

18. Miller, E. L.; Peterson, D.; Randolph, K.; Ainscough, C. In *Critical Metrics and Fundamental Materials Challenges for Renewable Hydrogen Production Technologies*, MRS Proceedings, Cambridge Univ Press: 2014; pp mrss14-1669-d01-02.

19. Timilsina, G. R.; Kurdgelashvili, L.; Narbel, P. A., Solar energy: Markets, economics and policies. *Renewable and Sustainable Energy Reviews* **2012,** *16* (1), 449-465.

20. Hug, H.; Bader, M.; Mair, P.; Glatzel, T., Biophotovoltaics: natural pigments in dye-sensitized solar cells. *Applied Energy* **2014,** *115*, 216-225.

21. Hagfeldt, A.; Boschloo, G.; Sun, L.; Kloo, L.; Pettersson, H., Dye-Sensitized Solar Cells. *Chemical Reviews* **2010,** *110* (11), 6595-6663.

22. Abdulrazzaq, O. A.; Saini, V.; Bourdo, S.; Dervishi, E.; Biris, A. S., Organic Solar Cells: A Review of Materials, Limitations, and Possibilities for Improvement. *Particulate Science & Technology* **2013,** *31* (5), 427-442.

23. Dennler, G.; Scharber, M. C.; Brabec, C. J., Polymer-Fullerene bulk-heterojunction solar cells. *Advanced Materials* **2009,** *21* (13), 1323-1338.

24. Lin, Y.; Li, Y.; Zhan, X., Small molecule semiconductors for high-efficiency organic photovoltaics. *Chemical Society Reviews* **2012,** *41* (11), 4245-4272.

25. Liu, Y.; Chen, C.-C.; Hong, Z.; Gao, J.; Yang, Y. M.; Zhou, H.; Dou, L.; Li, G.; Yang, Y., Solution-processed small-molecule solar cells: breaking the 10% power conversion efficiency. *Scientific reports* **2013,** *3*.

26. Zhang, L.; Cole, J. M., Anchoring Groups for Dye-Sensitized Solar Cells. *ACS Applied Materials & Interfaces* **2015,** *7* (6), 3427-3455.

27. Sengupta, D.; Das, P.; Mondal, B.; Mukherjee, K., Effects of doping, morphology and film-thickness of photo-anode materials for dye sensitized solar cell application–A review. *Renewable and Sustainable Energy Reviews* **2016,** *60*, 356-376.

28. Choy, W. C., *Organic Solar Cells*. Springer: 2013; Vol. 2.

29. Benanti, T. L.; Venkataraman, D., Organic solar cells: an overview focusing on active layer morphology. *Photosynthesis research* **2006,** *87* (1), 73-81.

30. Joly, D.; Pellejà, L.; Narbey, S.; Oswald, F.; Chiron, J.; Clifford, J. N.; Palomares, E.; Demadrille, R., A robust organic dye for dye sensitized solar cells based on iodine/iodide electrolytes combining high efficiency and outstanding stability. *Scientific reports* **2014,** *4*.

31. Heremans, P.; Cheyns, D.; Rand, B. P., Strategies for Increasing the Efficiency of Heterojunction Organic Solar Cells: Material Selection and Device Architecture. *Accounts of Chemical Research* **2009,** *42* (11), 1740-1747.

32. Mahmood, A., Triphenylamine based dyes for dye sensitized solar cells: A review. *Solar Energy* **2016,** *123*, 127-144.

33. Wood, J. D.; Jellison, J. L.; Finke, A. D.; Wang, L.; Plunkett, K. N., Electron Acceptors Based on Functionalizable Cyclopenta[hi]aceanthrylenes and Dicyclopenta[de,mn]tetracenes. *Journal of the American Chemical Society* **2012,** *134* (38), 15783-15789.

34. Smestad, G., Nanocrystalline Solar Cell Kit: Recreating Photosynthesis. *The Institute for Chemical Education, Madison, WI* **1998**.

35. Maiaugree, W.; Lowpa, S.; Towannang, M.; Rutphonsan, P.; Tangtrakarn, A.; Pimanpang, S.; Maiaugree, P.; Ratchapolthavisin, N.; Sang-aroon, W.; Jarernboon, W.; Amornkitbamrung, V., A dye sensitized solar cell using natural counter electrode and natural dye derived from mangosteen peel waste. *Scientific Reports* **2015,** *5*, 15230.

36. von Barth, U., Basic density-functional theory—an overview. *Physica Scripta* **2004,** *2004* (T109), 9.

37. Argaman, N.; Makov, G., Density functional theory: An introduction. *American Journal of Physics* **2000,** *68* (1), 69-79.

38. Jones, R. O., Density functional theory: Its origins, rise to prominence, and future. *Reviews of modern physics* **2015,** *87* (3), 897.

39. Cohen, A. J.; Mori-Sánchez, P.; Yang, W., Challenges for density functional theory. *Chemical Reviews* **2011,** *112* (1), 289-320.

40. Orio, M.; Pantazis, D. A.; Neese, F., Density functional theory. *Photosynthesis Research* **2009,** *102* (2), 443-453.

41. Frisch, M. J.; Trucks, G. W.; Schlegel, H. B.; Scuseria, G. E.; Robb, M. A.; Cheeseman, J. R.; Scalmani, G.; Barone, V.; Mennucci, B.; Petersson, G. A.; Nakatsuji, H.; Caricato, M.; Li, X.; Hratchian, H. P.; Izmaylov, A. F.; Bloino, J.; Zheng, G.; Sonnenberg, J. L.; Hada, M.; Ehara, M.; Toyota, K.; Fukuda, R.; Hasegawa, J.; Ishida, M.; Nakajima, T.; Honda, Y.; Kitao, O.; Nakai, H.; Vreven, T.; Montgomery Jr., J. A.; Peralta, J. E.; Ogliaro, F.; Bearpark, M. J.; Heyd,

J.; Brothers, E. N.; Kudin, K. N.; Staroverov, V. N.; Kobayashi, R.; Normand, J.; Raghavachari, K.; Rendell, A. P.; Burant, J. C.; Iyengar, S. S.; Tomasi, J.; Cossi, M.; Rega, N.; Millam, N. J.; Klene, M.; Knox, J. E.; Cross, J. B.; Bakken, V.; Adamo, C.; Jaramillo, J.; Gomperts, R.; Stratmann, R. E.; Yazyev, O.; Austin, A. J.; Cammi, R.; Pomelli, C.; Ochterski, J. W.; Martin, R. L.; Morokuma, K.; Zakrzewski, V. G.; Voth, G. A.; Salvador, P.; Dannenberg, J. J.; Dapprich, S.; Daniels, A. D.; Farkas, Ö.; Foresman, J. B.; Ortiz, J. V.; Cioslowski, J.; Fox, D. J. *Gaussian 09*, Gaussian, Inc.: Wallingford, CT, USA, 2009.

42. Chase, D. T.; Fix, A. G.; Rose, B. D.; Weber, C. D.; Nobusue, S.; Stockwell, C. E.; Zakharov, L. N.; Lonergan, M. C.; Haley, M. M., Electron-Accepting 6, 12-Diethynylindeno [1, 2-b] fluorenes: Synthesis, Crystal Structures, and Photophysical Properties. *Angewandte Chemie International Edition* **2011,** *50* (47), 11103-11106.

43. Koper, C.; Sarobe, M.; Jenneskens, L. W., Redox properties of non-alternant cyclopenta-fused polycyclic aromatic hydrocarbons: The effect of peripheral pentagon annelation. *Physical Chemistry Chemical Physics* **2004,** *6* (2), 319-327.

44. Lafleur, A. L.; Howard, J. B.; Taghizadeh, K.; Plummer, E. F.; Scott, L. T.; Necula, A.; Swallow, K. C., Identification of C20H10 dicyclopentapyrenes in flames: correlation with corannulene and fullerene formation. *The Journal of Physical Chemistry* **1996,** *100* (43), 17421-17428.

45. Seiders, T. J.; Elliott, E. L.; Grube, G. H.; Siegel, J. S., Synthesis of corannulene and alkyl derivatives of corannulene. *Journal of the American Chemical Society* **1999,** *121* (34), 7804-7813.

46. Wang, T.; Weerasinghe, K. C.; Ubaldo, P. C.; Liu, D.; Li, W.; Zhou, X.; Wang, L., Tuning electron–hole distance of the excitons in organic molecules using functional groups. *Chemical Physics Letters* **2015,** *618*, 142-146.

47. Ubaldo, P. C.; Colley, N. D.; Plunkett, K. N.; Wang, L., Electron Acceptability of Cyclopenta-fused Polycyclic Aromatic Hydrocarbons: Effect of One Electron. *unpublished work*. 2015.

48. Scharber, M. C.; Mühlbacher, D.; Koppe, M.; Denk, P.; Waldauf, C.; Heeger, A. J.; Brabec, C. J., Design rules for donors in bulk-heterojunction solar cells—Towards 10% energy-conversion efficiency. *Advanced Materials* **2006,** *18* (6), 789-794.

49. Ubaldo, P. C.; Harrell, B. L.; Zhang, Q.; Colley, N. D.; Dick, B., J; Wang, L., The Best Functionals to Predict Optoelectronic Properties of MTPA Derivatives. *unpublished work*. 2015.

50. Association, W. C. The Coal Resource. http://www.worldcoal.org/. (accessed 04/2016).

51. Association, I. C. What is coal? http://www.ilcoalassn.com/what-is-coal-.html. (accessed 04/2016).

52. Survey, K. G. Classification and Rank of Coal https://www.uky.edu/KGS/coal/coalkinds.htm. (accessed 04/2016).

53. Education, K. C. Coal and The Illinois Economy http://www.coaleducation.org/lessons/sec/Illinois/ilecon.htm. (accessed 04/2016).

54. Emery, K.; Osterwald, C., Solar cell efficiency measurements. *Solar Cells* **1986,** *17* (2), 253-274.